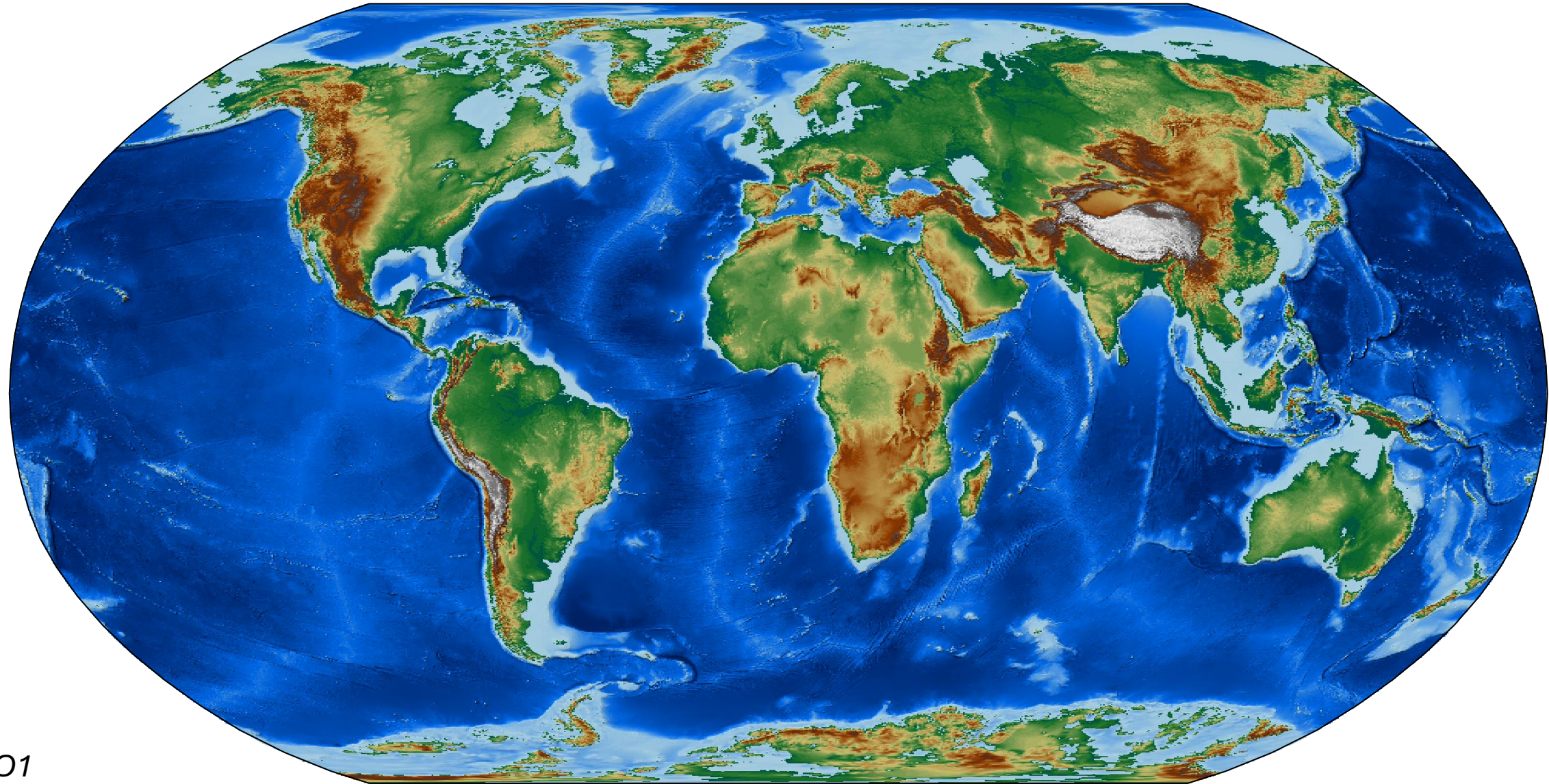
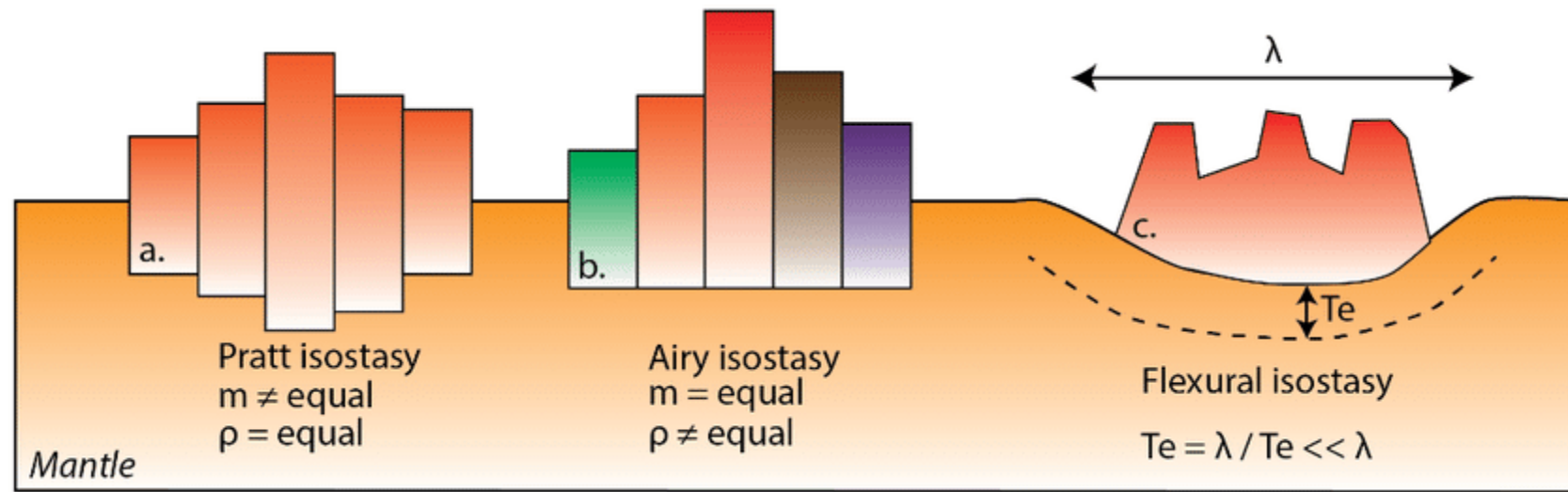


Mantle Convection and Dynamic Topography

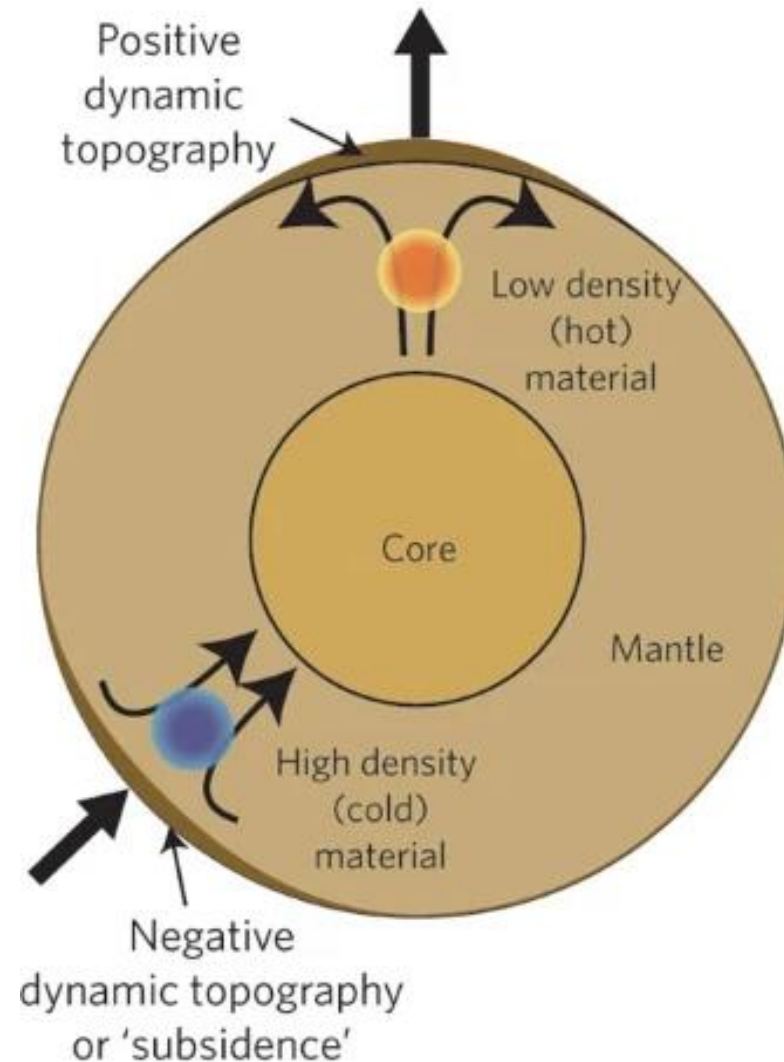
April 2, 2024

Earth's topography

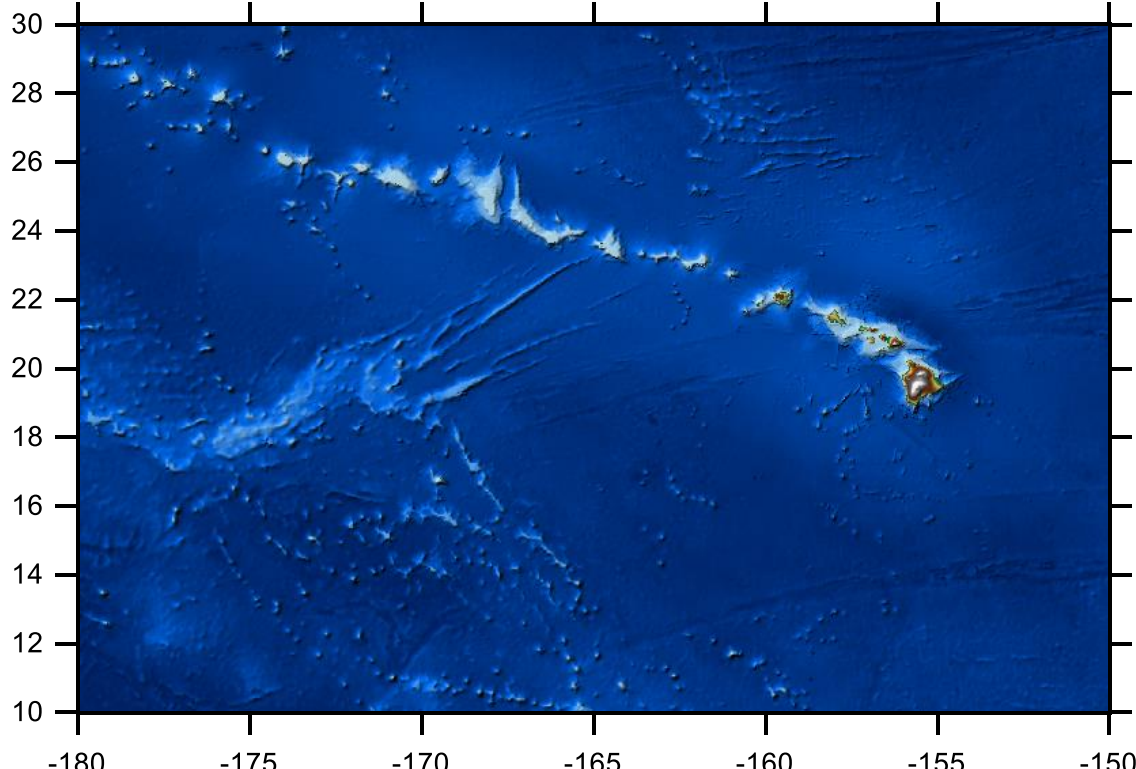




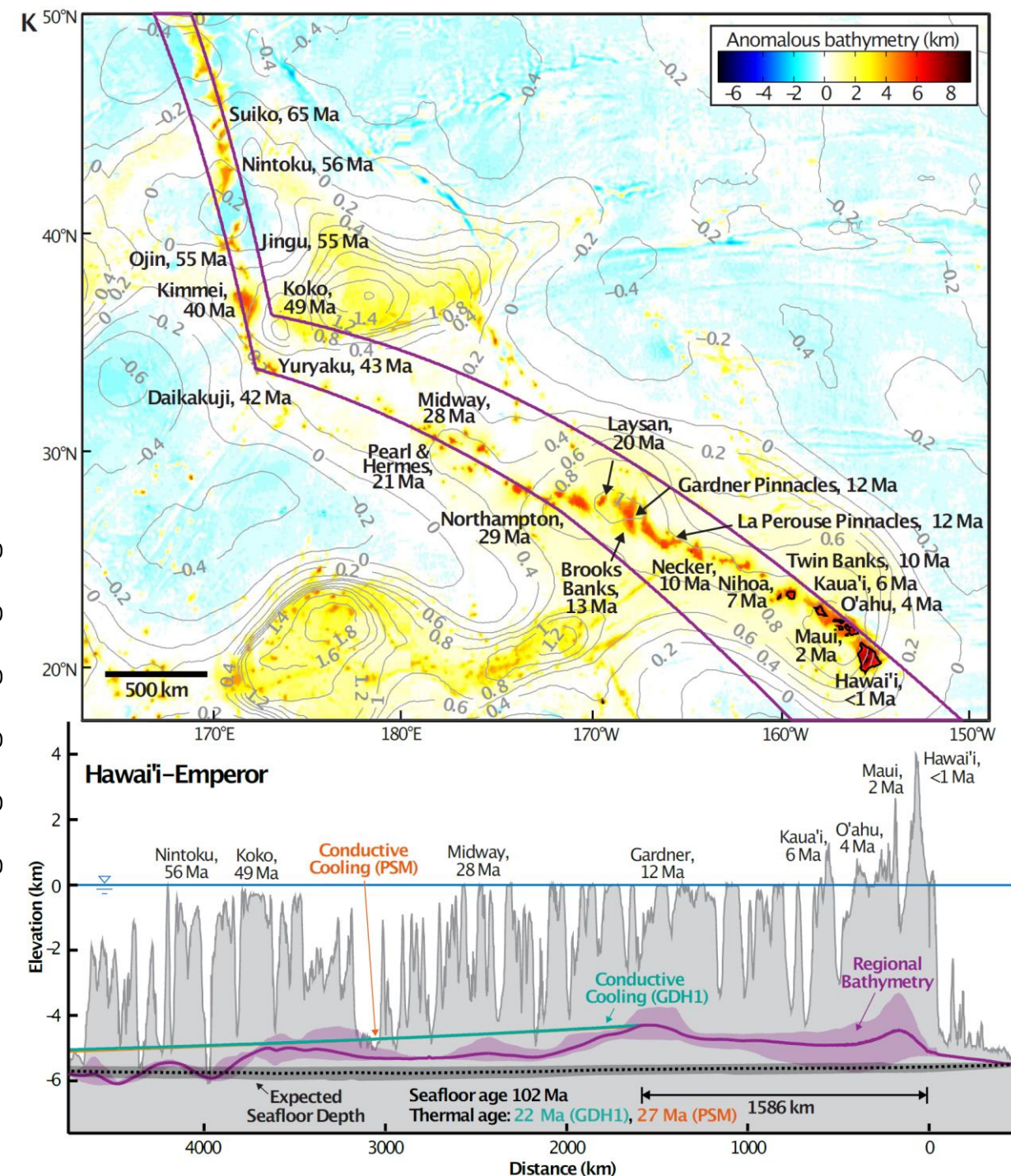
Mantle dynamic topography



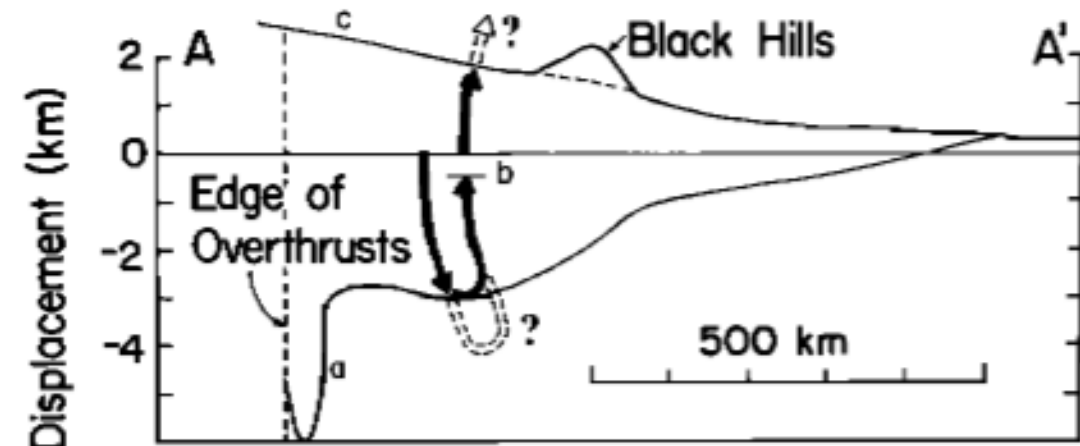
Hawaiian Swell



Huppert et al., 2020



Western Interior Seaway



Early beginnings

THERMAL CONVECTION IN THE INTERIOR OF THE EARTH

Chaim L. Pekeris, D.Sc.

(Communicated by Dr. Harold Jeffreys)

(Received 1935 December 12)

The general nature of the distortion of the crust can be seen at once. Over the rising current it will be pushed upwards and it will be pulled downwards over the sinking currents.

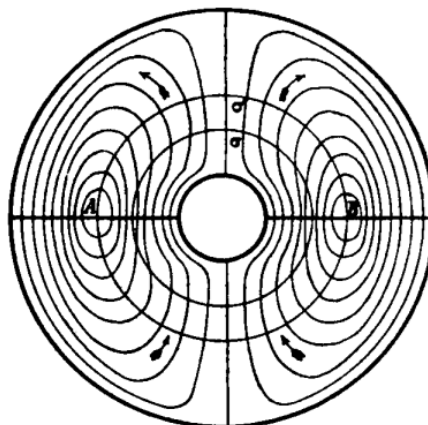
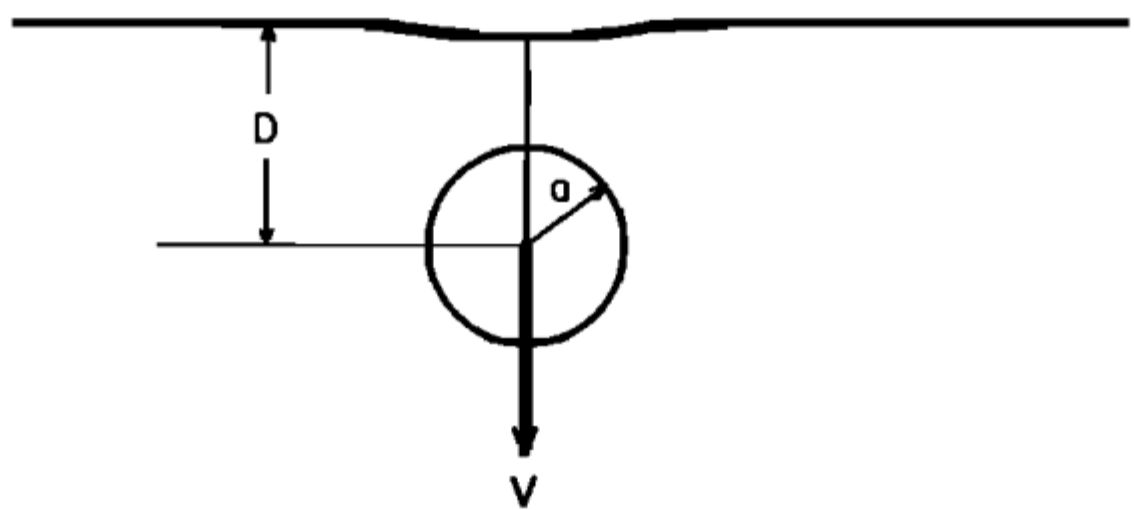


FIG 1.—Stream lines in a fluid contained between concentric spheres, the inner having the higher temperature. (After Oberbeck.)

Theory

$$\sigma_N(x, 0) = 2g \delta\rho a^3 \frac{D^3}{D^2 + x^2}^{\frac{5}{2}}$$

$$DT = \frac{\sigma_N}{\Delta\rho g}$$



Theory

TECTONICS, VOL. 8, NO. 5, PAGES 1079-1094, OCTOBER 1989

TILTING OF CONTINENTAL INTERIORS BY THE DYNAMICAL EFFECTS OF SUBDUCTION

J. X. Mitrovica

Department of Physics, University of Toronto, Toronto,
Ontario, Canada

C. Beaumont

Department of Oceanography, Dalhousie University,
Halifax, Nova Scotia, Canada

G. T. Jarvis

Department of Earth and Atmospheric Science, York
University, North York, Ontario, Canada

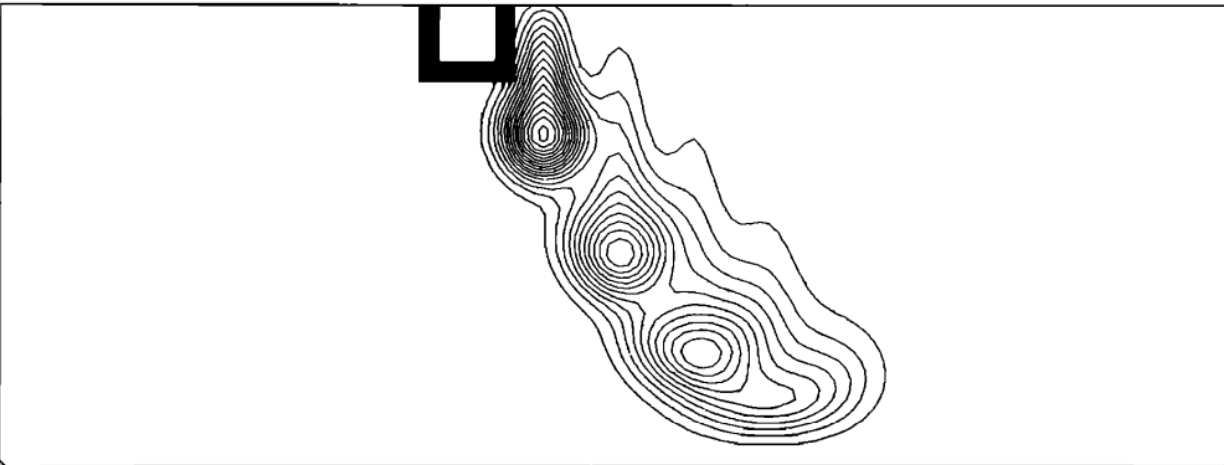


Fig. 10. The thermal field produced by superimposing the $t = 0.0, 0.25, 0.50, 0.75$, and 1.0 fields of the model of Figure 6 ($\Delta t = 0.25$, see text). Each field is horizontally shifted, with respect to the previous field, by an amount equal to the width of the initial block (116 km); only a portion of the cell is shown. The near-surface dip of the resulting subduction is approximately 45° .

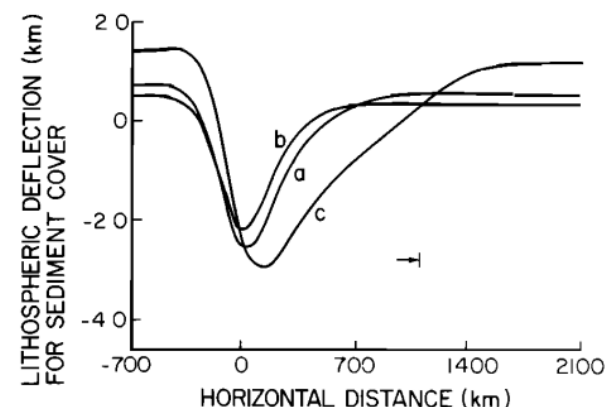
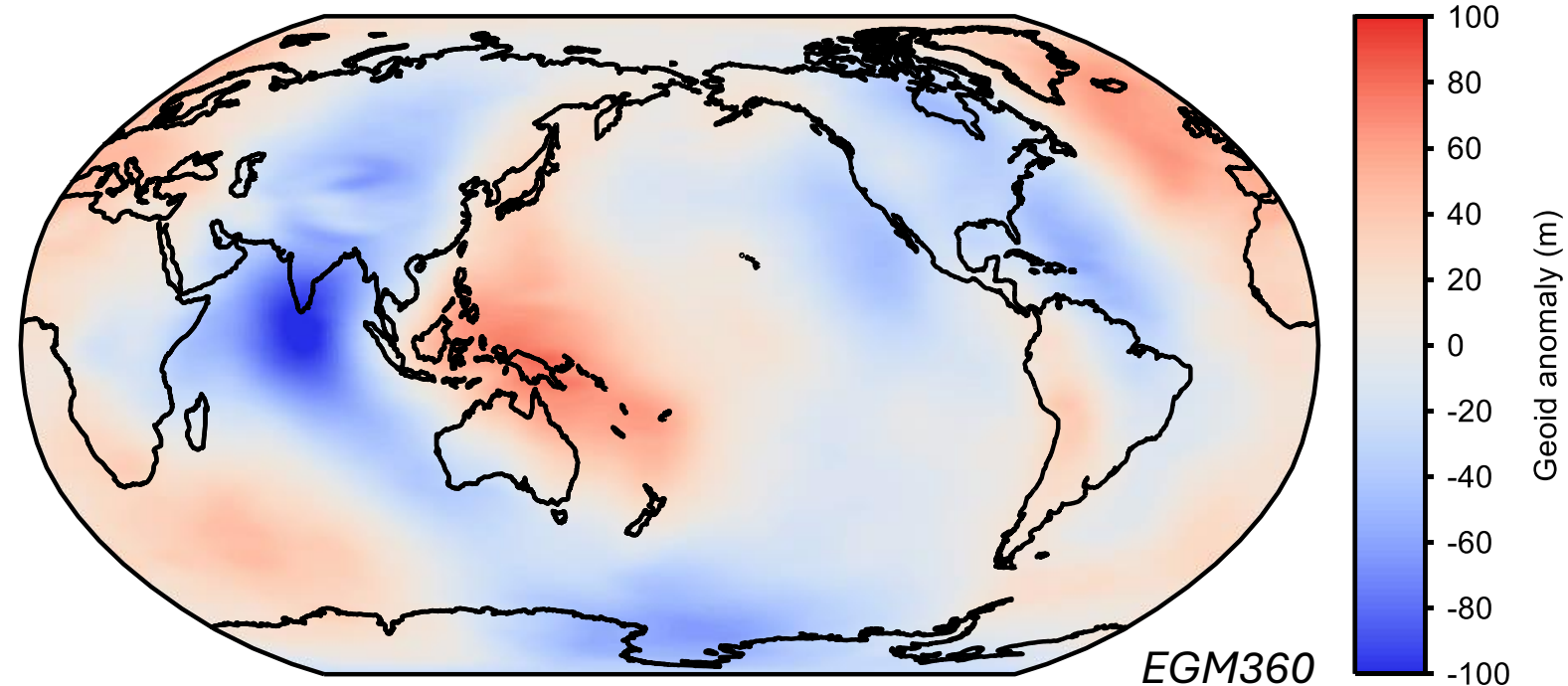


Fig. 11. The topographic profile corresponding to the field of Figure 10 (labeled a). Also shown are the deflections for the cases of near surface dips of 60° ($\Delta t = 0.33$, labeled b) and 30° ($\Delta t = 0.12$, labelled c). In all cases, $D = 5 \times 10^{23}$ Nm. The arrow gives the position of the right boundary of Figure 10.

Evidence – long-wavelength geoid

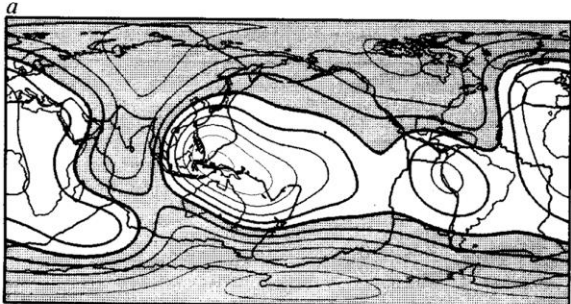
The anomalies in gravity are due to two effects working in opposite directions. Considering the subcontinental region, we have a positive contribution to gravity * due to the rise of the upper surface of the crust and, to a smaller degree, due to the rise of the boundaries between the crust and shell and between the shell and core, at each of which there is an increase in density. There is also a negative contribution to gravity on account of the lower density of the subcontinental matter caused by the assumed temperature perturbation.†

Pekeris, 1935



Evidence – long-wavelength geoid

Observed



Observed, slabs removed

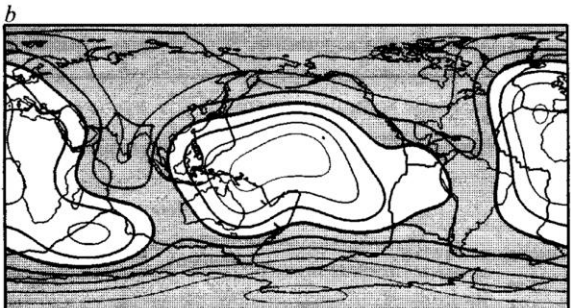
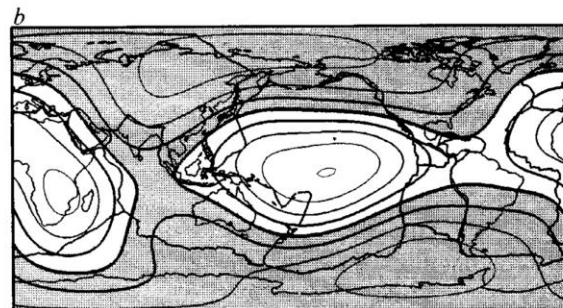
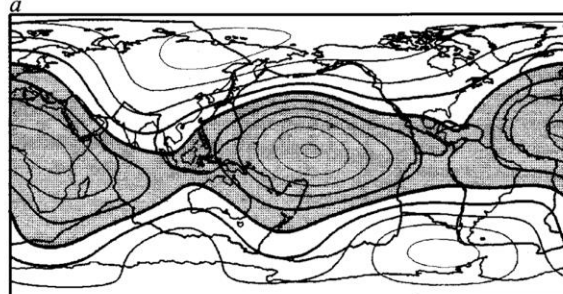


Fig. 2 *a*, The observed geoid¹³ for $l=2-6$ referred to the hydrostatic figure of the Earth. Geoid lows are shaded and the contour interval is 20 m. In all our maps, we show plate boundaries and continents for reference. *b*, The residual geoid for $l=2-6$ obtained by subtracting the effects of subducted slabs¹⁰. Lows are shaded; the contour interval is 20 m.

Density anomalies only



Density anomalies only + dynamic topography

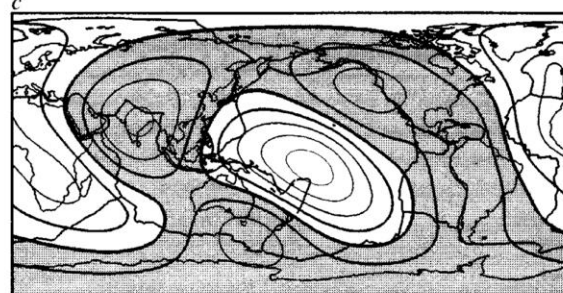
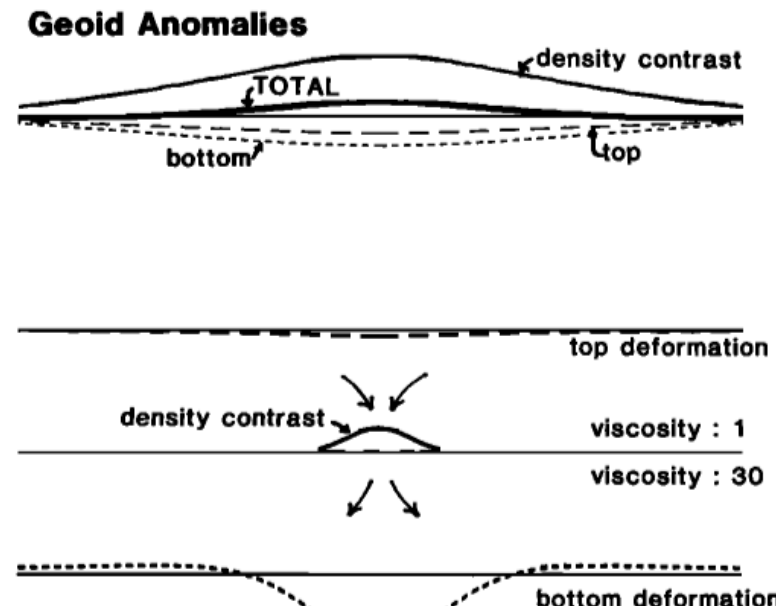
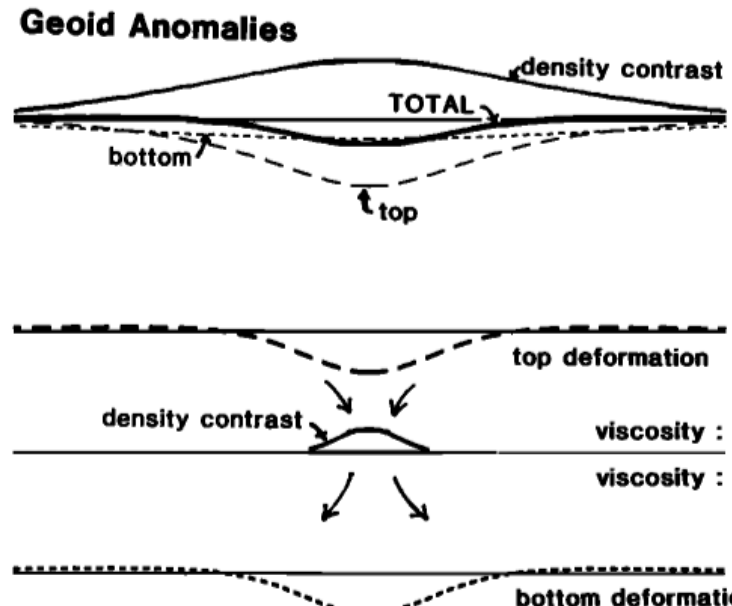
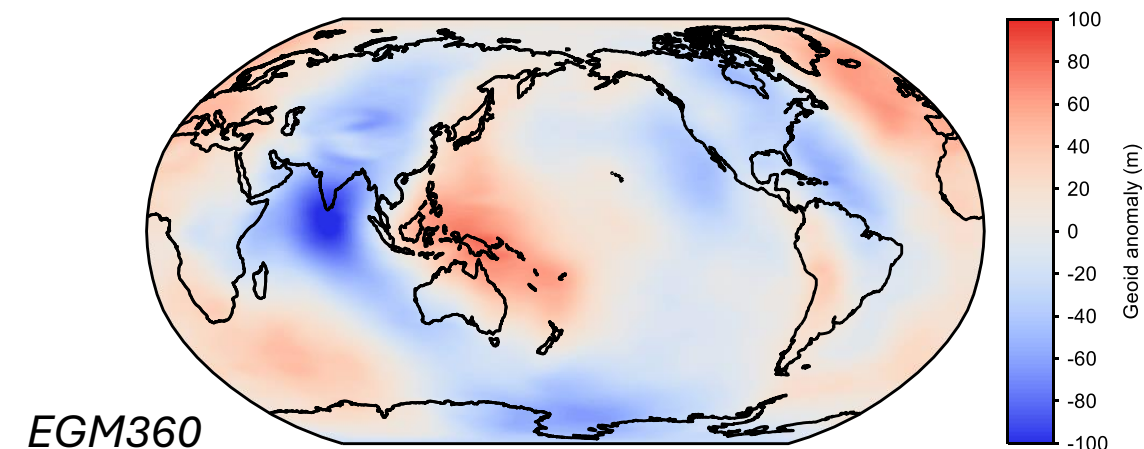


Fig. 3 Geoids calculated by applying dynamic response functions, such as those in Fig. 1, to the seismic models. *a*, CC-S, a static model (boundary deformation is not included); contour interval, 50 m. *b*, CC-U10, for a uniform composition model with a factor of 10 increase in lower mantle viscosity. *c*, Dz-U10, as *b*; contour intervals, 20 m. Lows are shaded.

Evidence – geoid at subduction zones



Hager, 1984

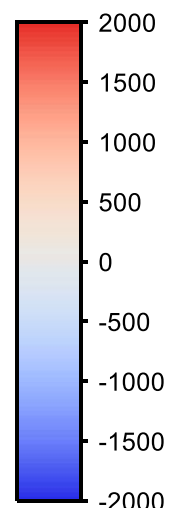
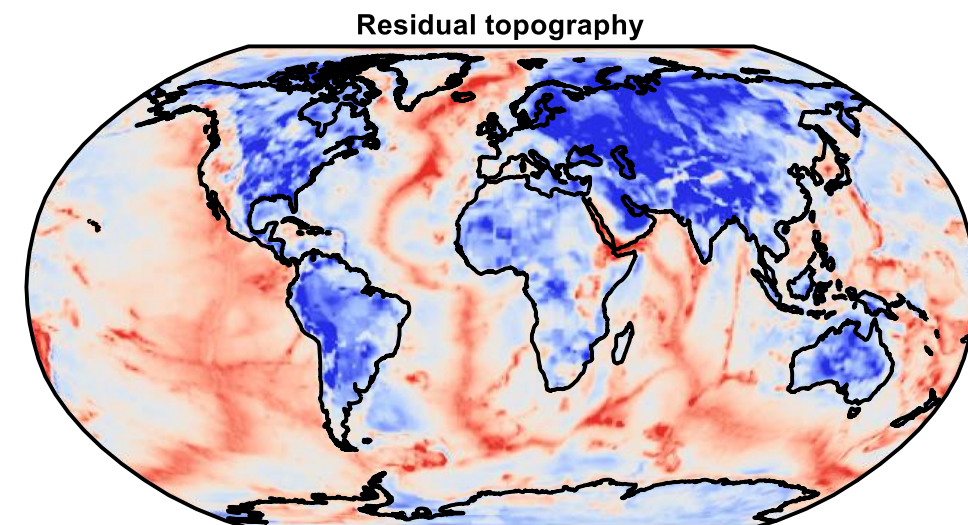
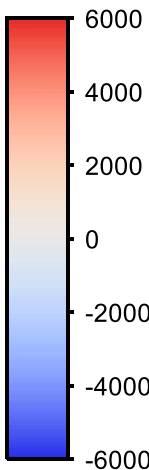
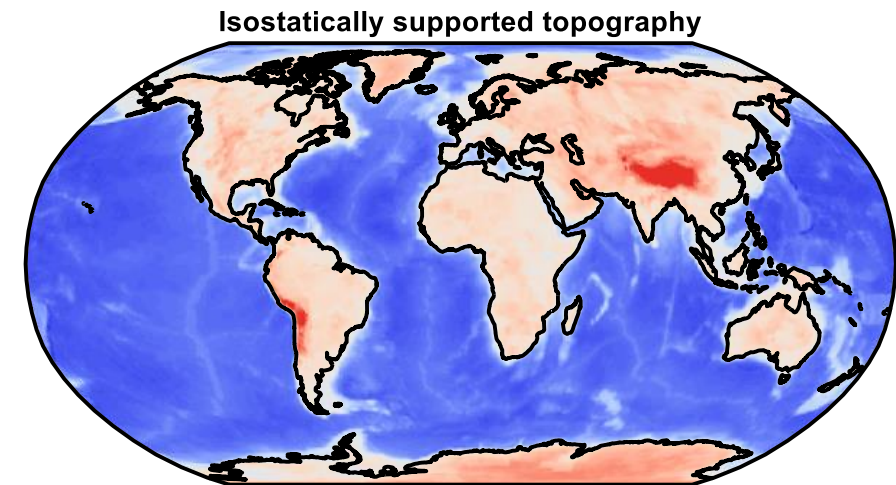
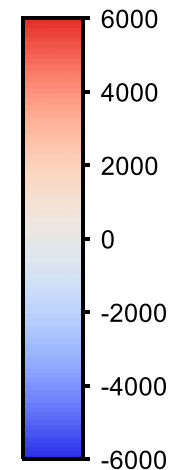
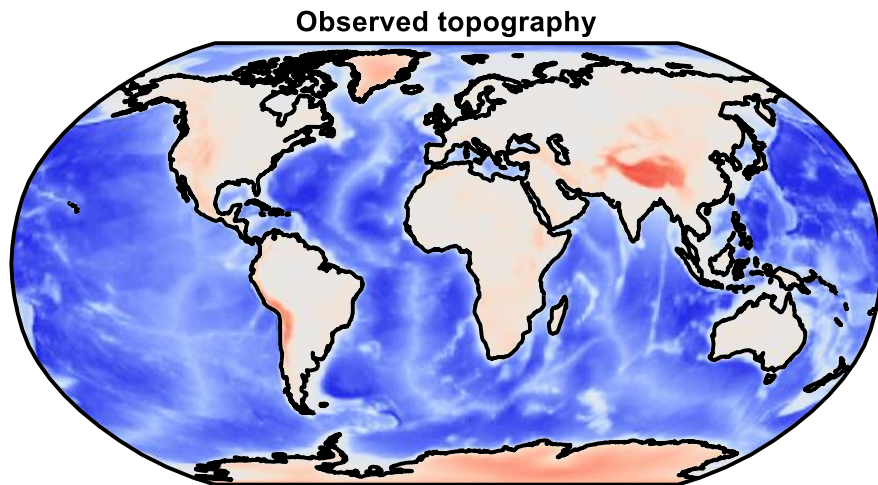


Observational constraints on present-day magnitude

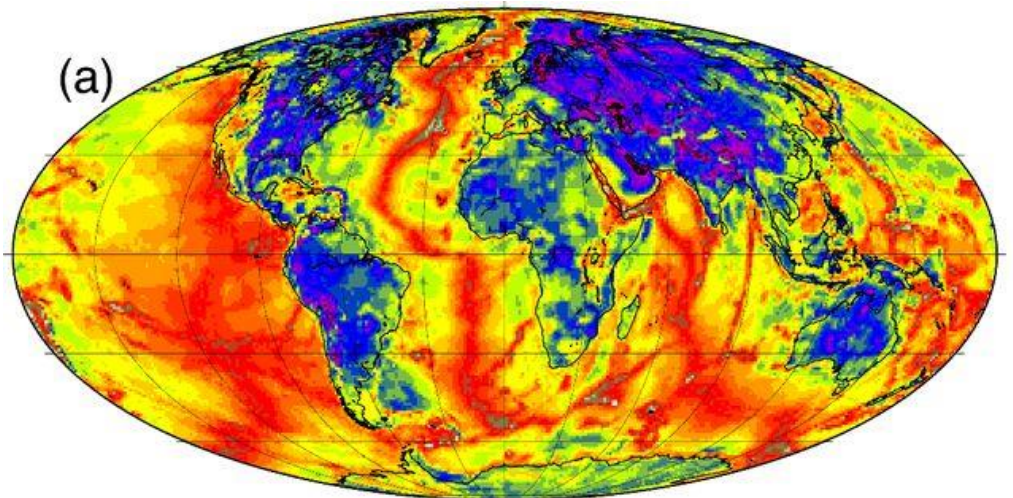
- “Residual” topography – topography that is not explained by isostasy

$$RT = T_{obs} - T_{iso} = T_{obs} - \int_0^{D_C} \frac{\rho_m - \rho(z)}{\rho_m} dz$$

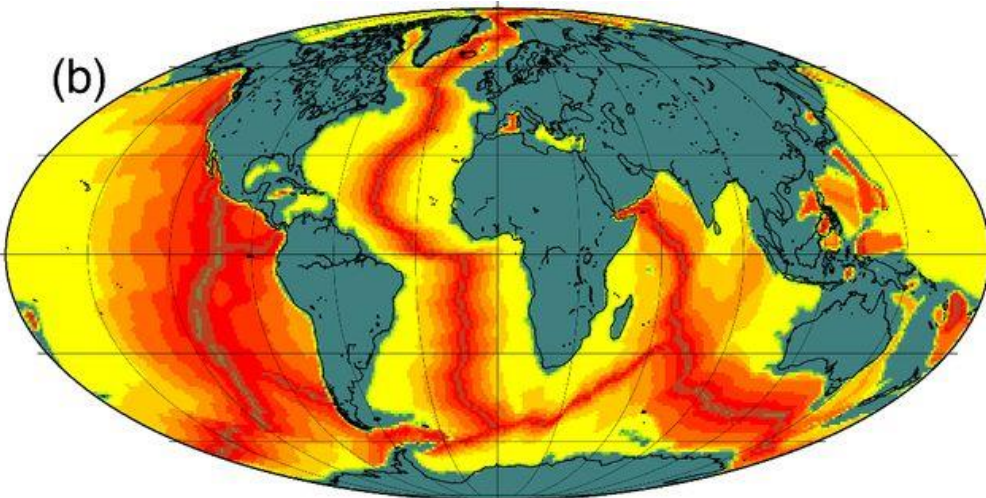
$$RT = T_{obs} - T_{iso} = T_{obs} - \int_0^{D_C} \frac{\rho_m - \rho(z)}{\rho_m} dz$$



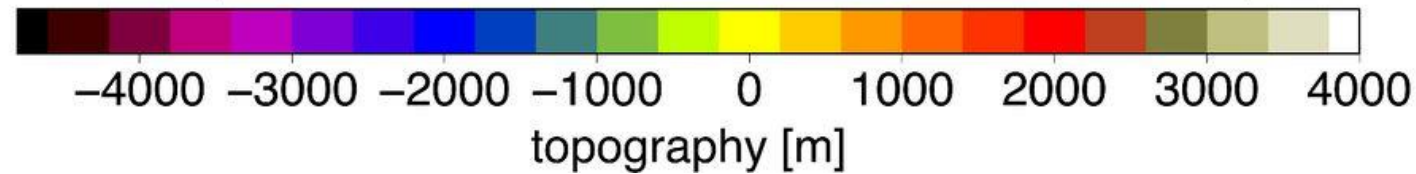
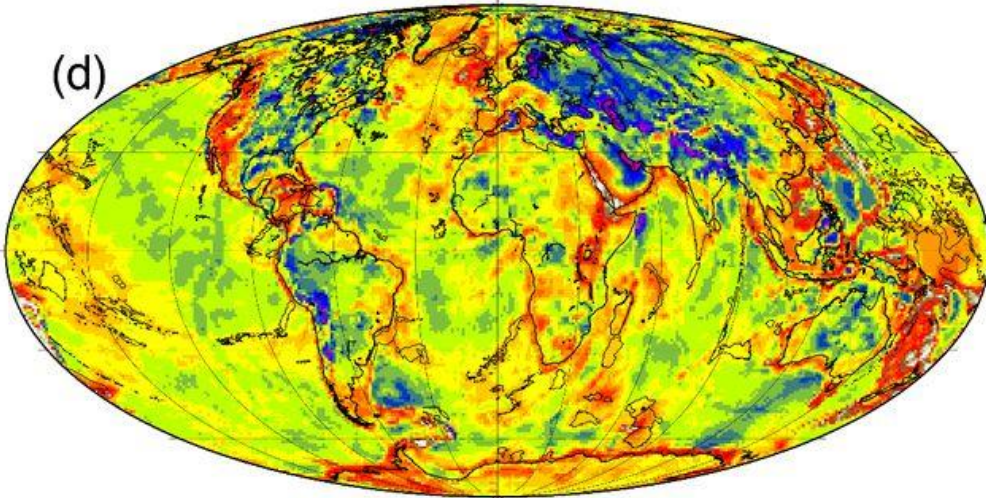
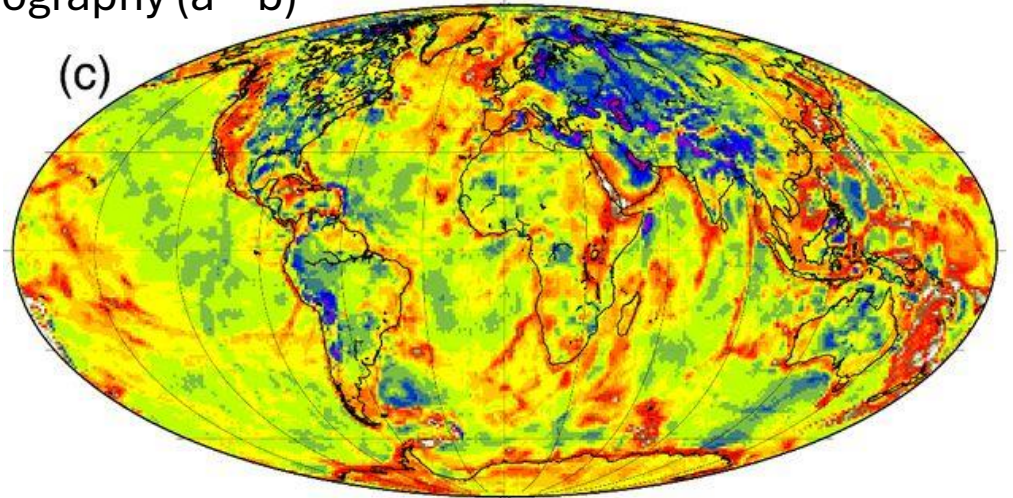
Non-isostatic topography,
from CRUST1.0 to Moho

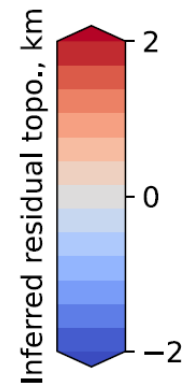
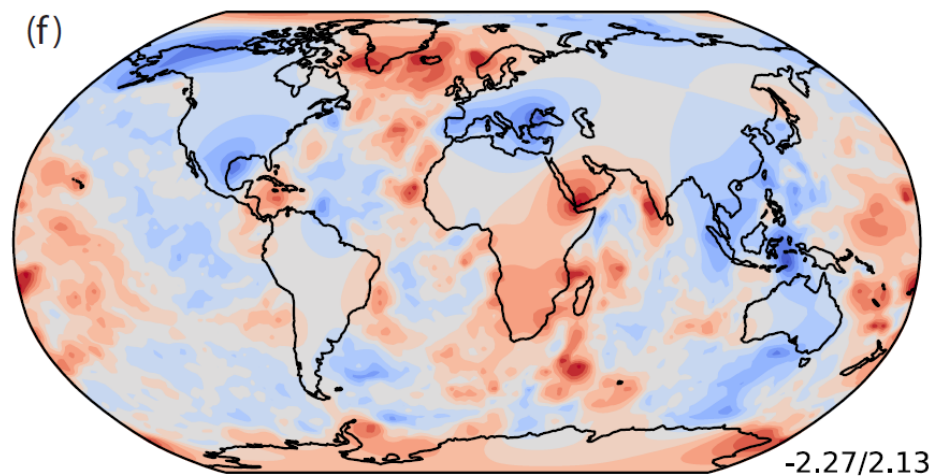
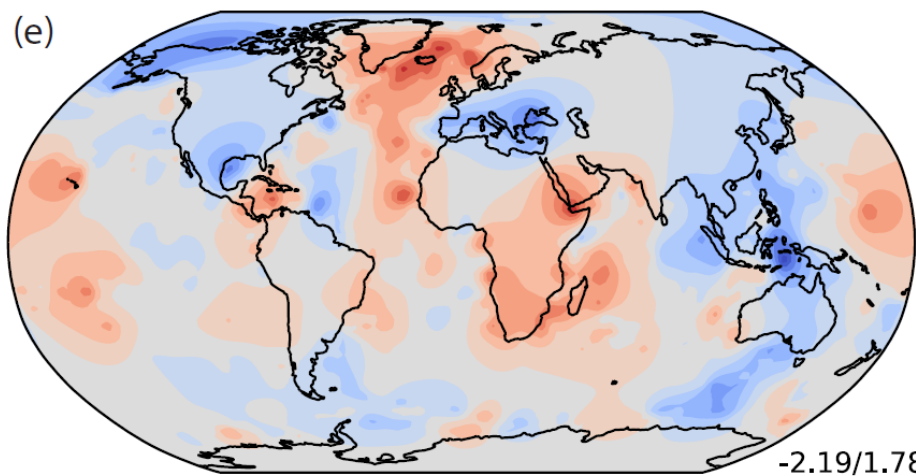
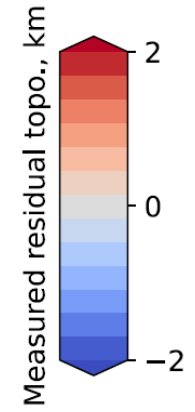
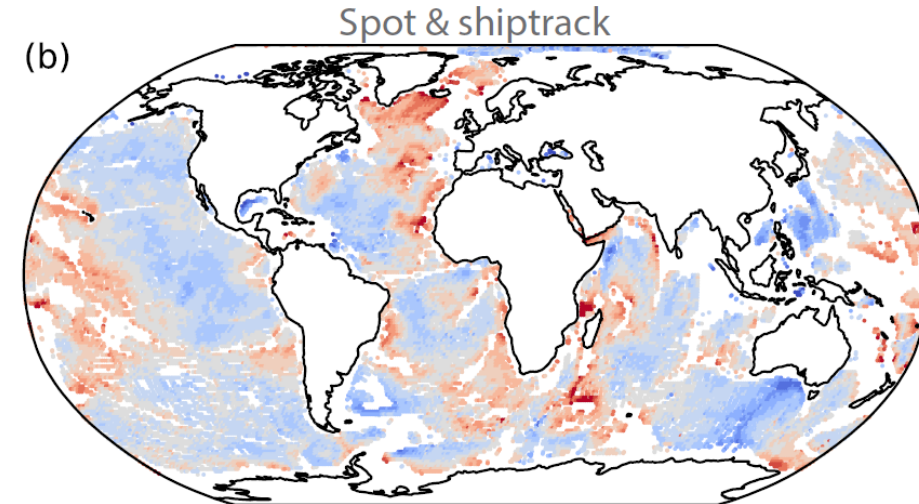
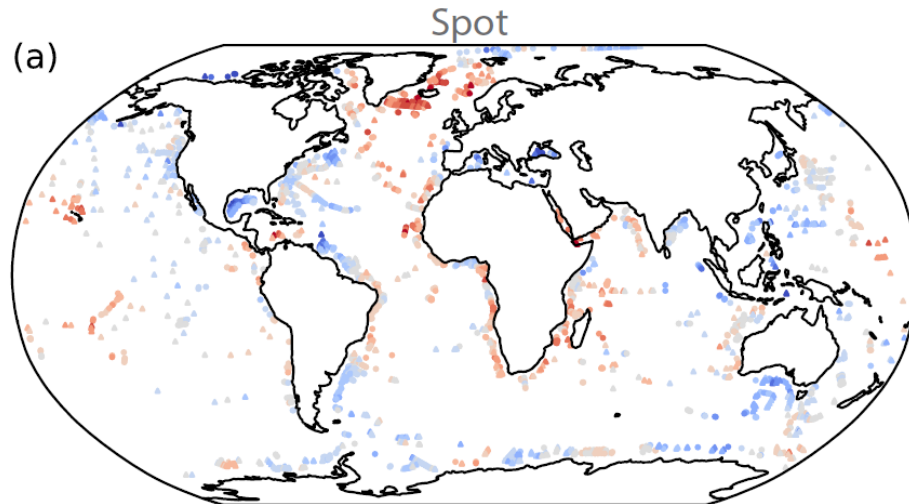


Ocean floor topography
calculated from crustal age

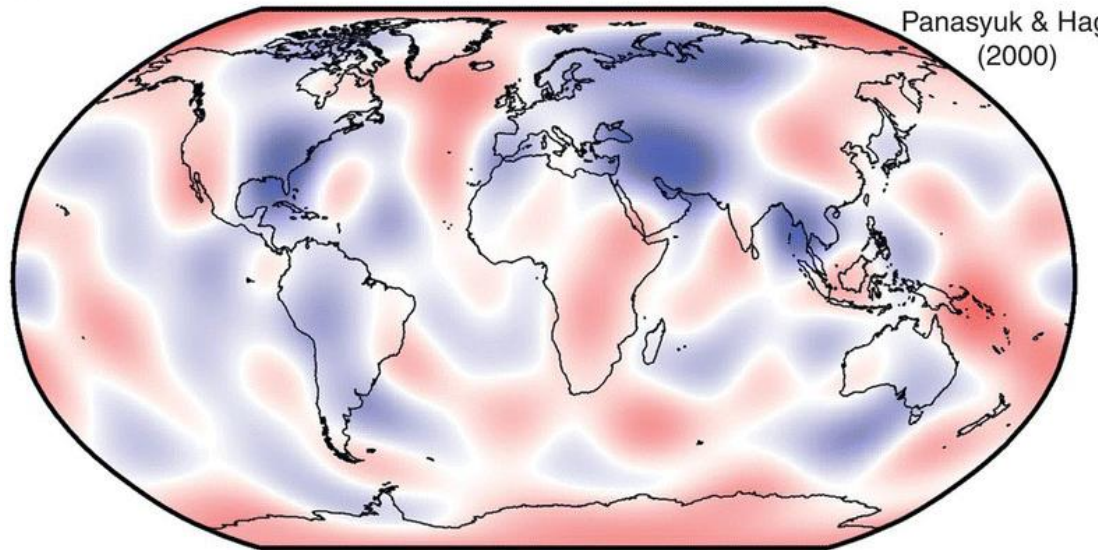


Residual topography (a – b)

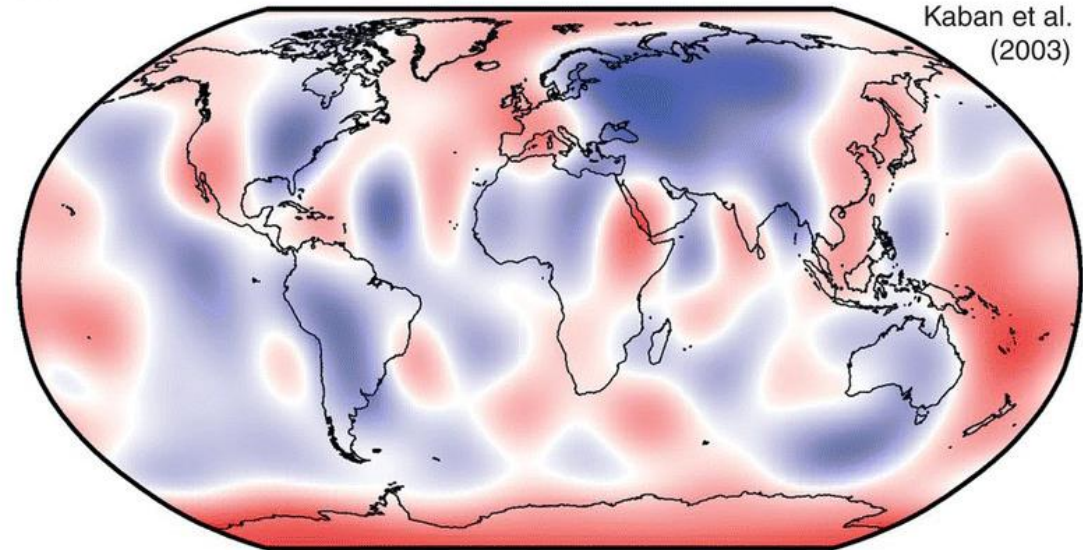




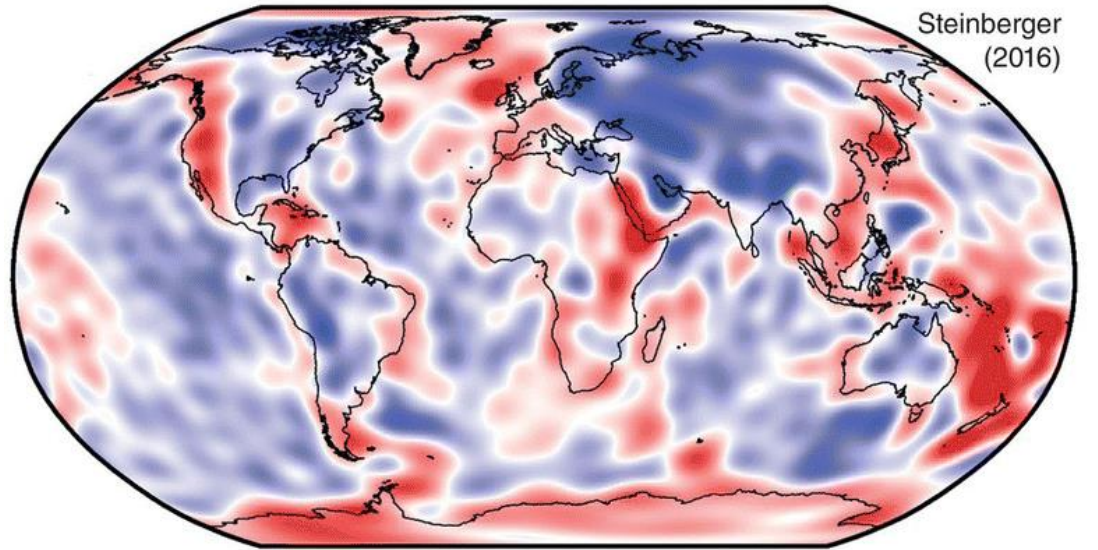
(b)



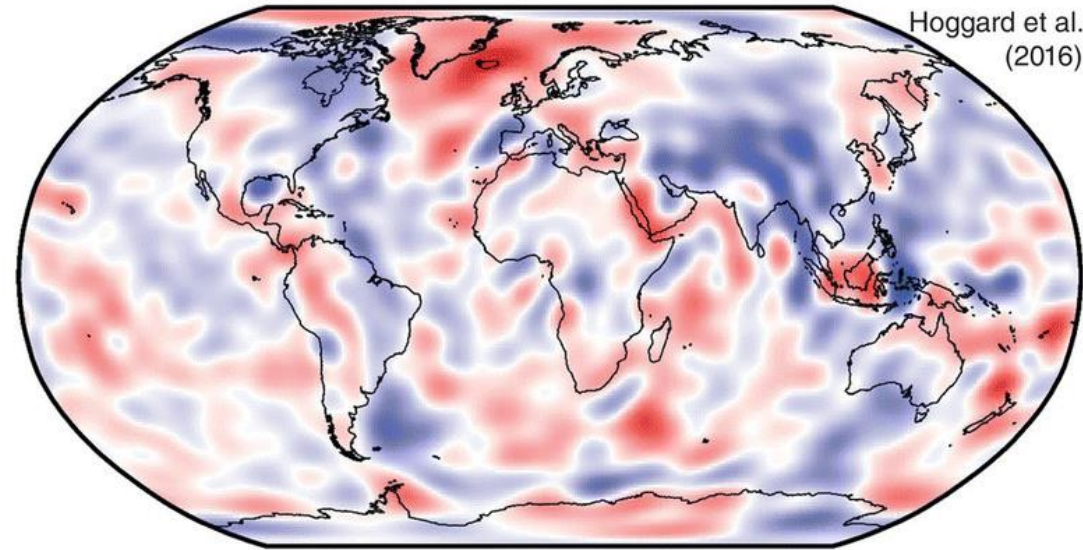
(c)



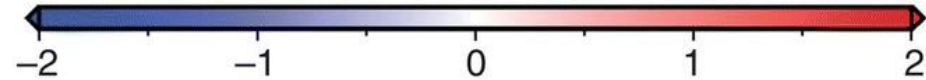
(d)

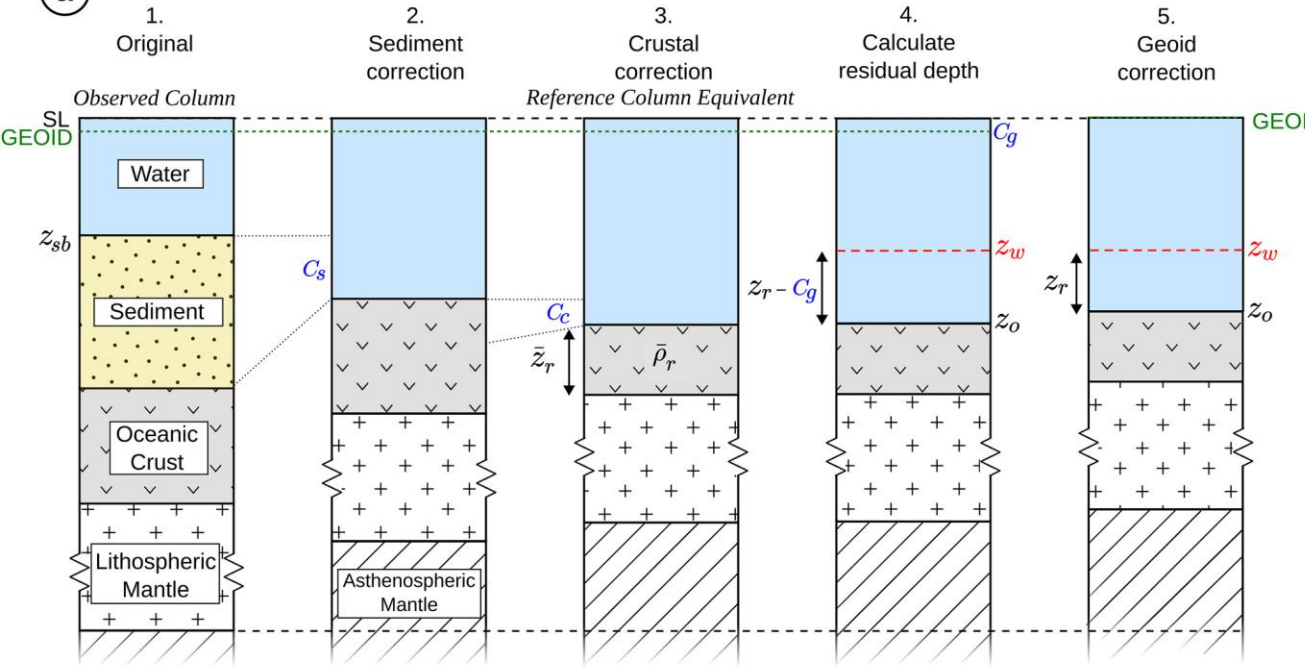


(e)

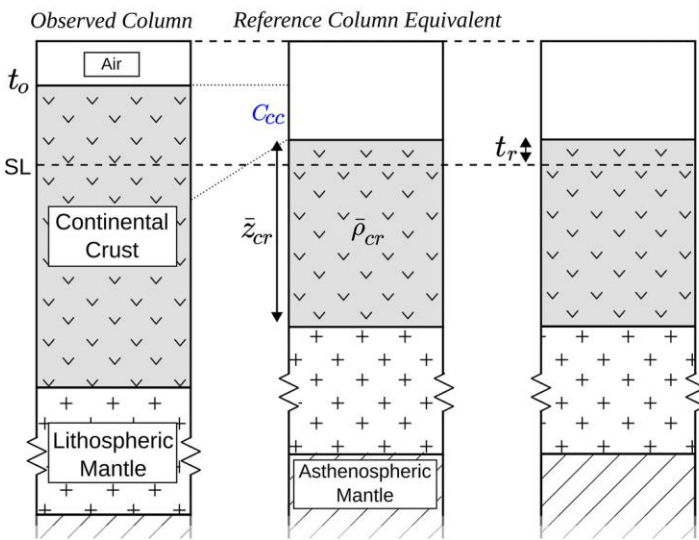


Residual Topography (km)



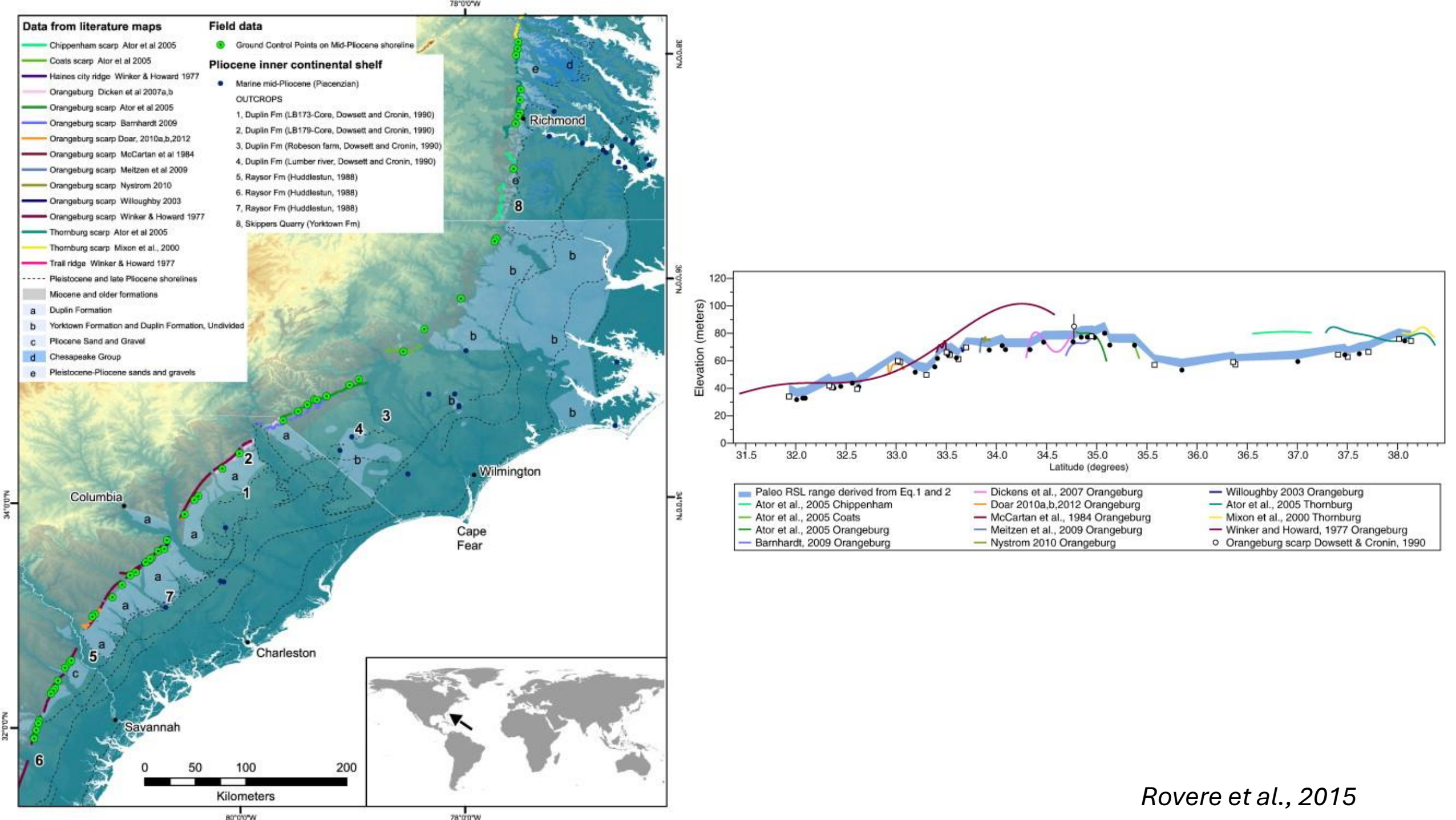
a OCEANIC CORRECTIONS**b CONTINENTAL CORRECTIONS**

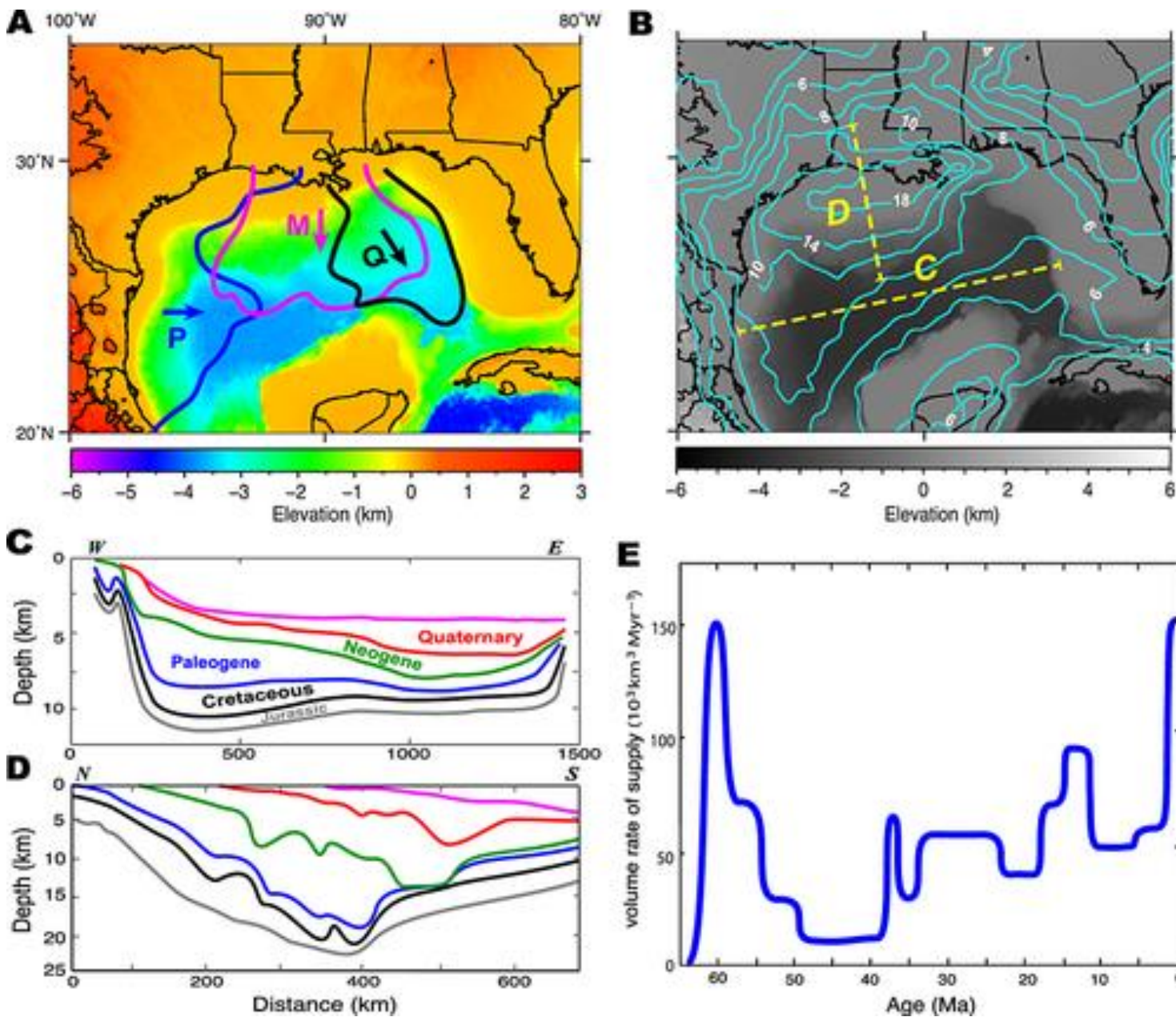
1. Original 2. Crustal correction 3. Calculate residual elevation
- Observed Column** **Reference Column Equivalent**



Geologic constraints on DT change

- Warped paleo-shorelines
- Sediment accumulation/depocenters
- Difficulties:
 - Long-wavelength
 - Slowly changing





Modeling dynamic topography

Regional

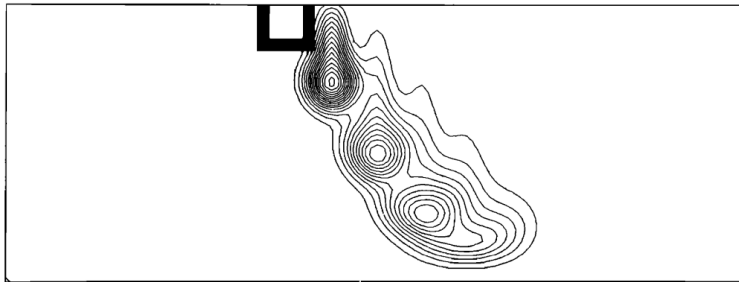


Fig. 10. The thermal field produced by superimposing the $t = 0.0, 0.25, 0.50, 0.75$, and 1.0 fields of the model of Figure 6 ($\Delta t = 0.25$, see text). Each field is horizontally shifted, with respect to the previous field, by an amount equal to the width of the initial block (116 km); only a portion of the cell is shown. The near-surface dip of the resulting subduction is approximately 45° .

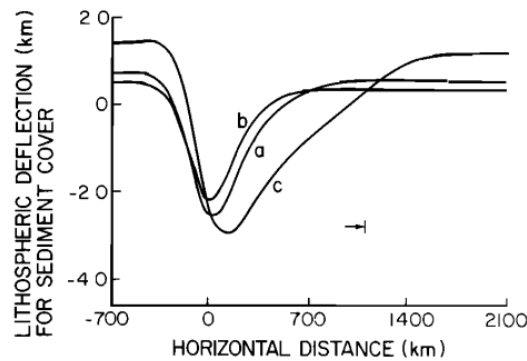


Fig. 11. The topographic profile corresponding to the field of Figure 10 (labeled a). Also shown are the deflections for the cases of near surface dips of 60° ($\Delta t = 0.33$, labeled b) and 30° ($\Delta t = 0.12$, labelled c). In all cases, $D = 5 \times 10^{23}$ Nm. The arrow gives the position of the right boundary of Figure 10.

Global

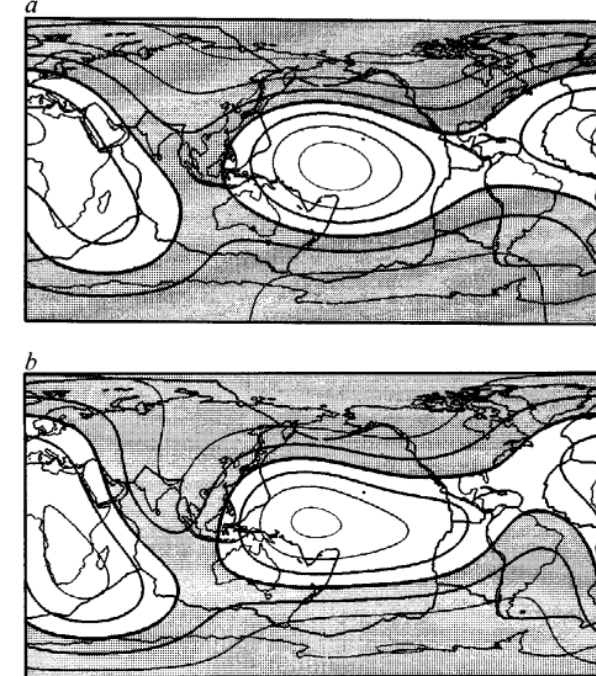
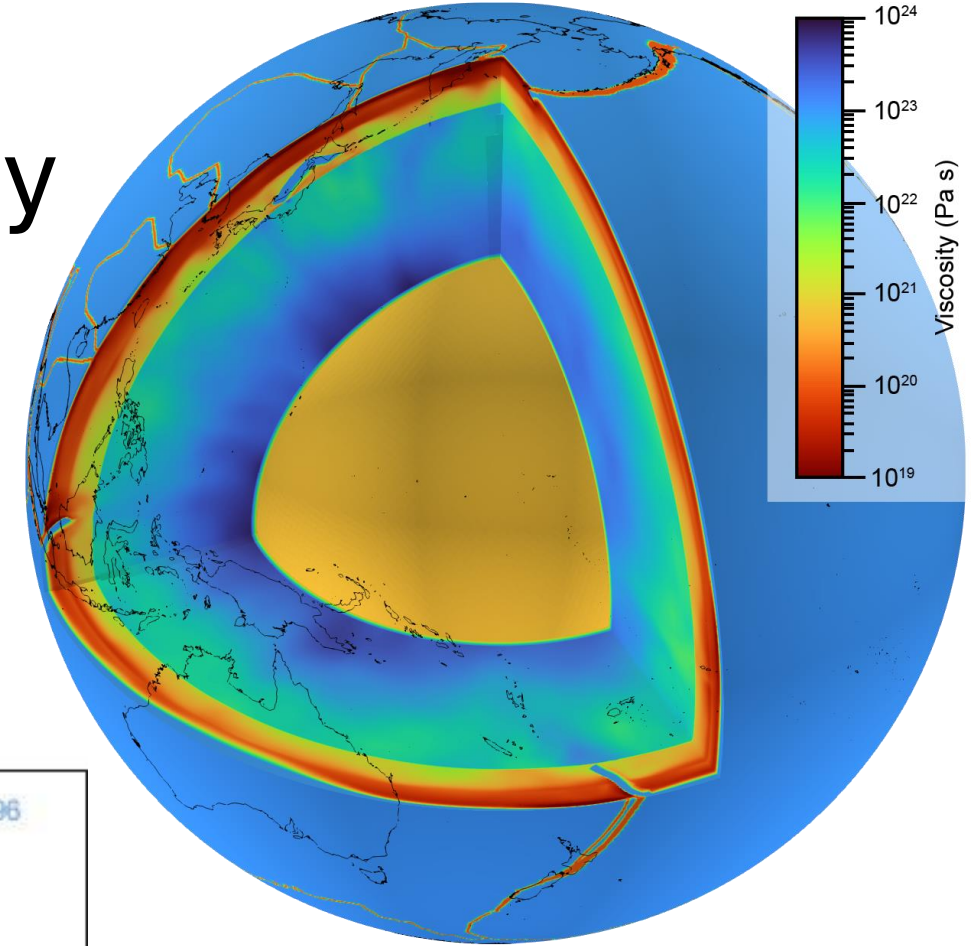
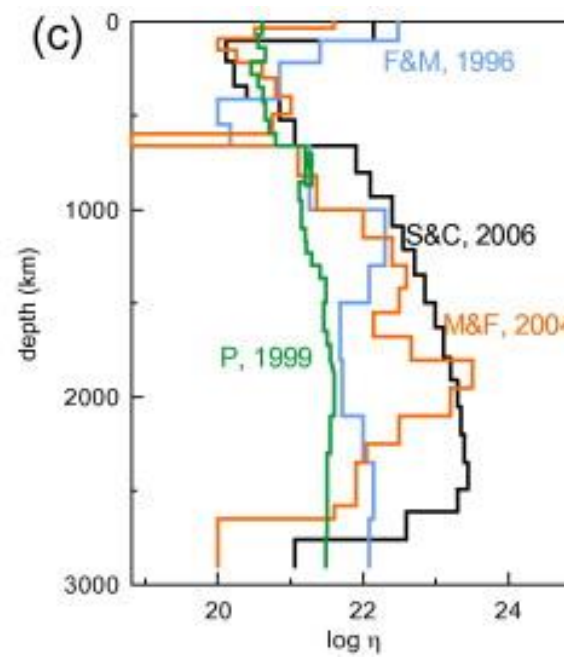


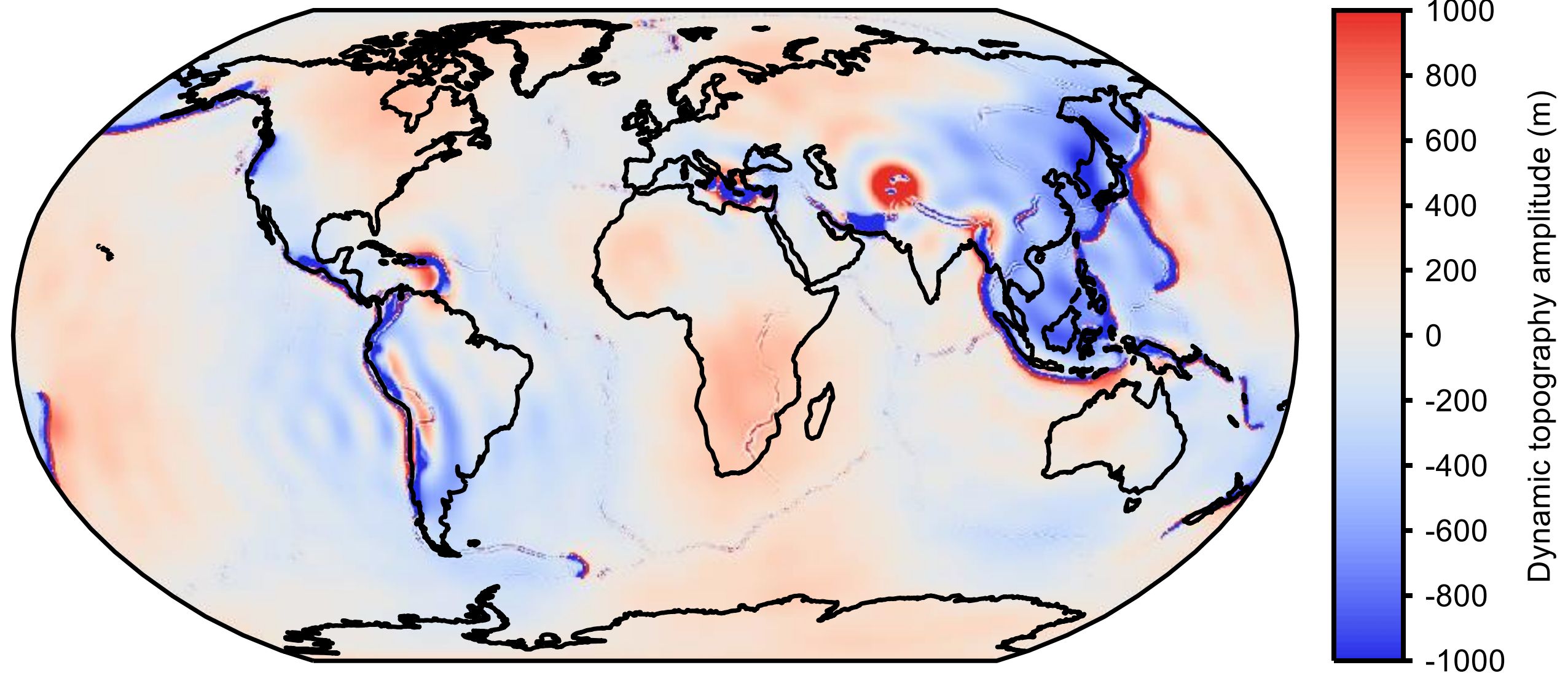
Fig. 4 Calculated topography for $l = 2-3$, a, at the surface and b, core-mantle boundary for the model CC-U10, which matches the geoid. Surface topography was calculated assuming a density contrast of 2.3 g cm^{-3} (appropriate for sub-oceanic regions). Topography at the core-mantle boundary is calculated for a density contrast of 4.5 g cm^{-3} across the interface. Lows are shaded. Contour intervals: a, 250 m; b, 500 m.

Modeling dynamic topography

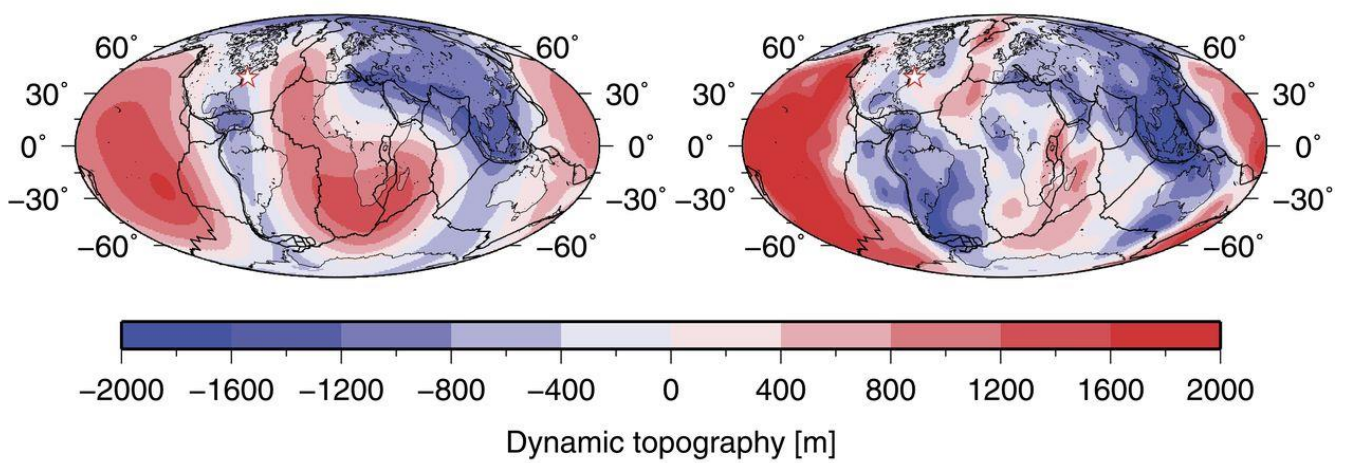
- Ingredients:
 - Mantle thermal structure
(seismic tomography, etc.)
 - Mantle rheology
- Compute:
 - Flow field
 - Surface normal stresses

$$DT = \frac{\sigma_N}{\Delta \rho g}$$

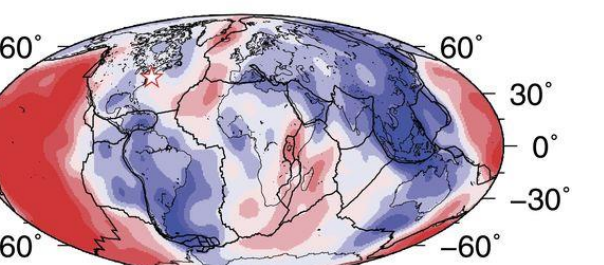




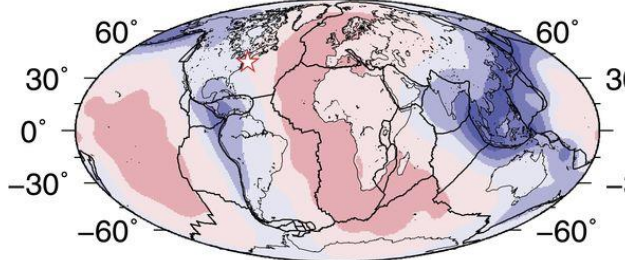
A. This study



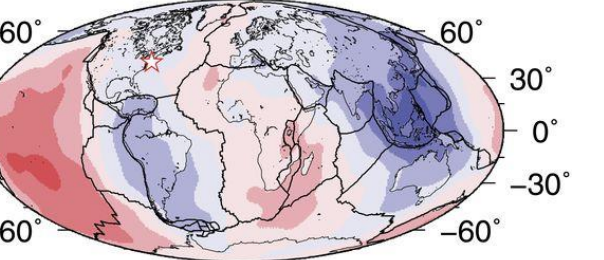
B. Steinberger (2007)



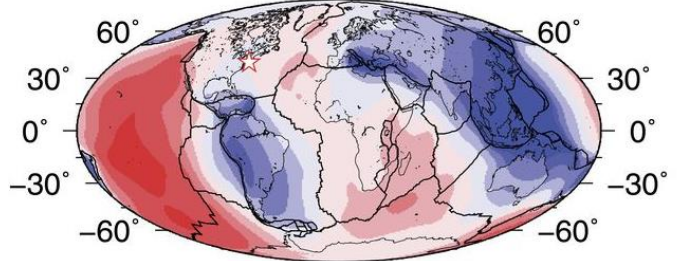
C. Ricard et al. (1993)



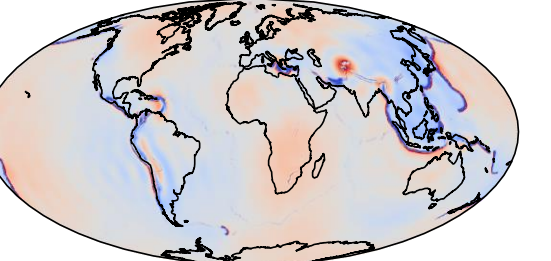
D. Conrad and Husson (2009)



E. Spasojevic and Gurnis (2012)

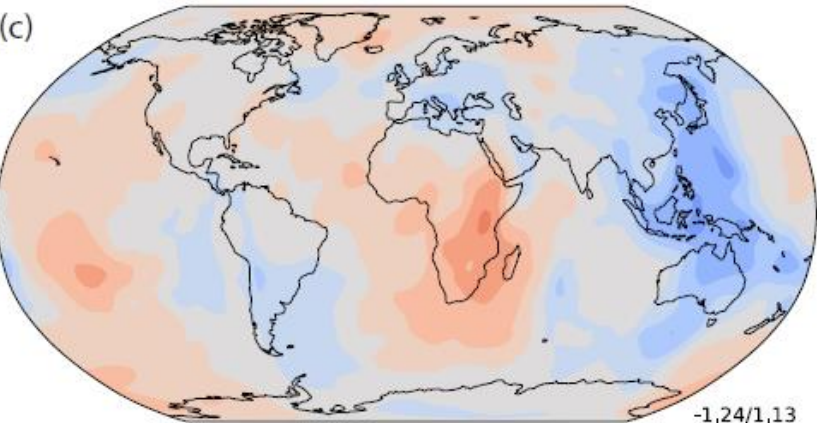


Goldberg and Holt

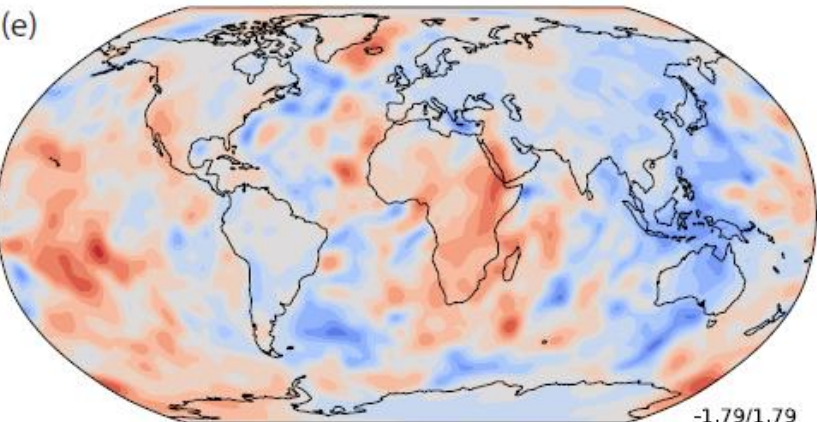


Flament et al., 2013

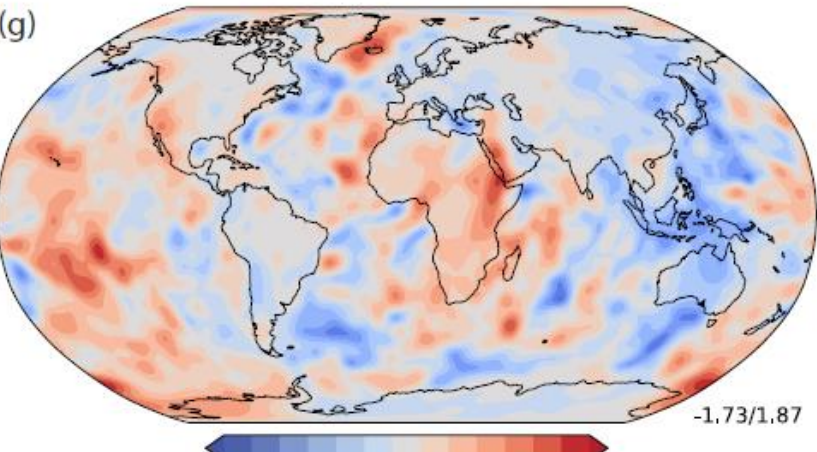
(c)



(e)

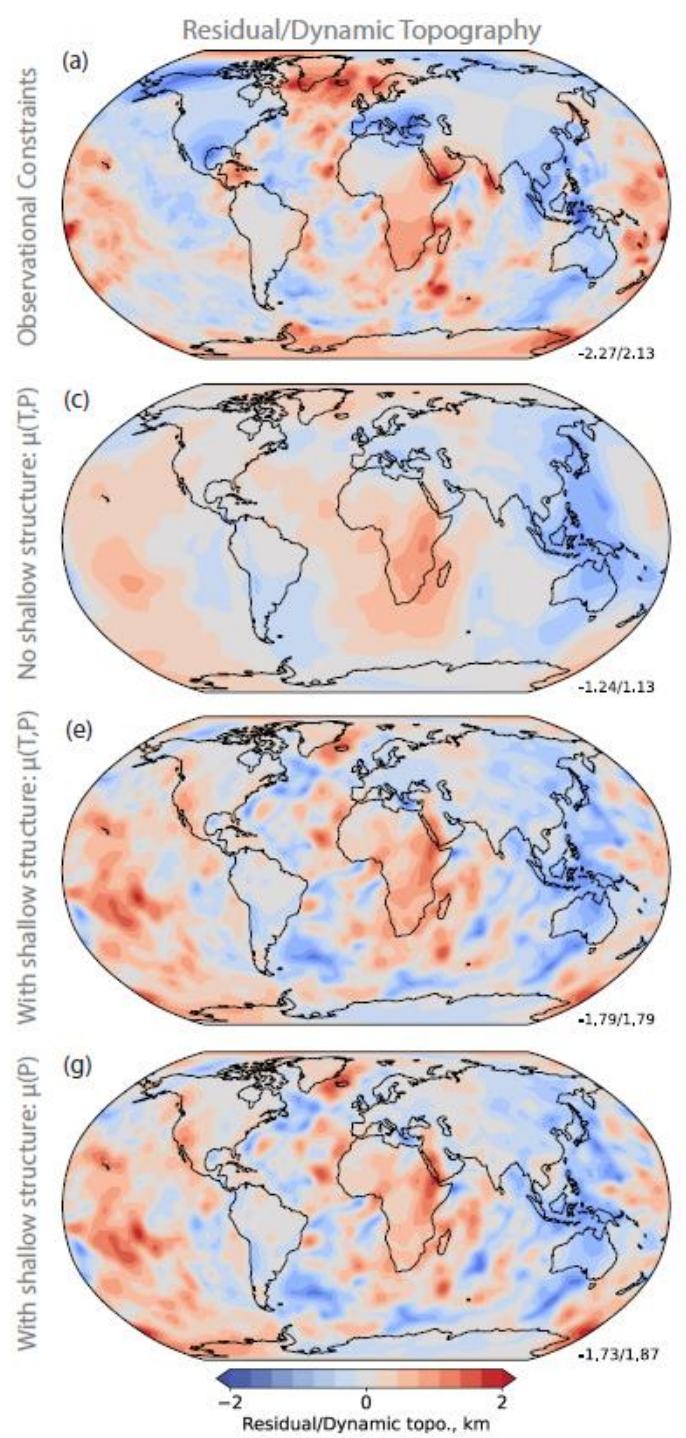


(g)



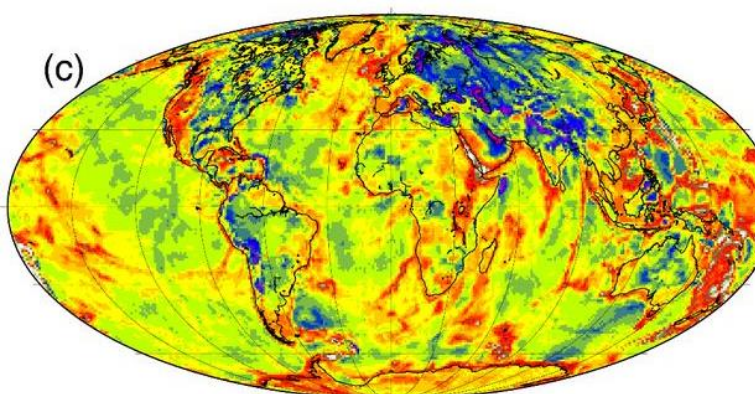
Davies et al., 2023

-2 0 2
Residual/Dynamic topo., km



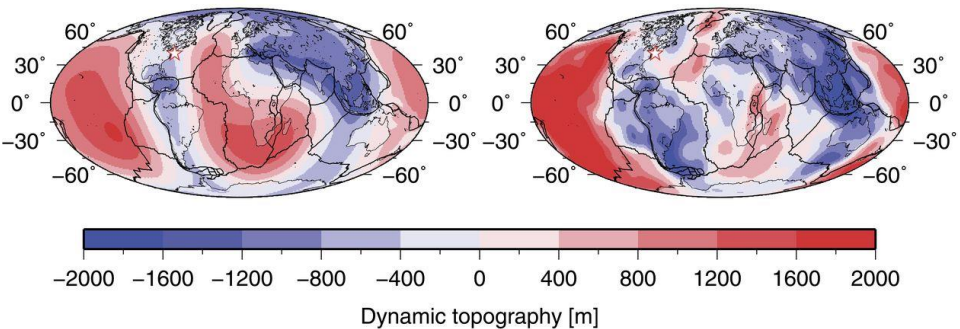
“Observed”

Models



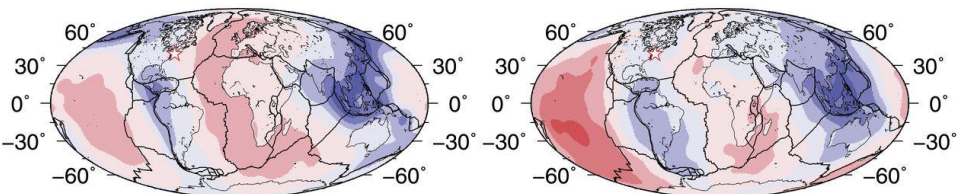
A. This study

B. Steinberger (2007)

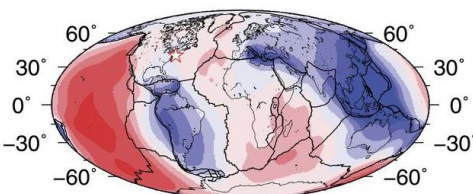


C. Ricard et al. (1993)

D. Conrad and Husson (2009)

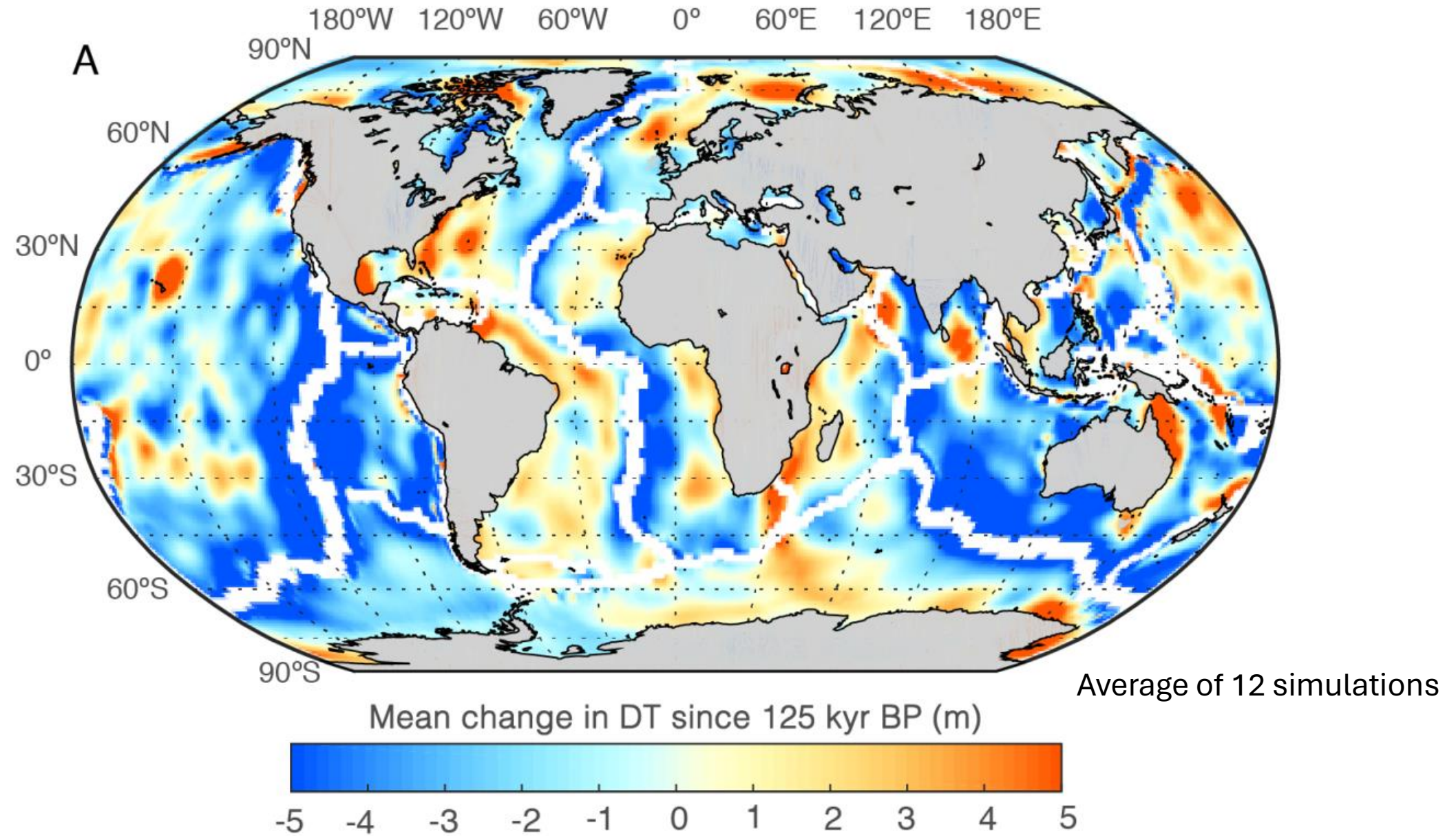


E. Spasojevic and Gurnis (2012)

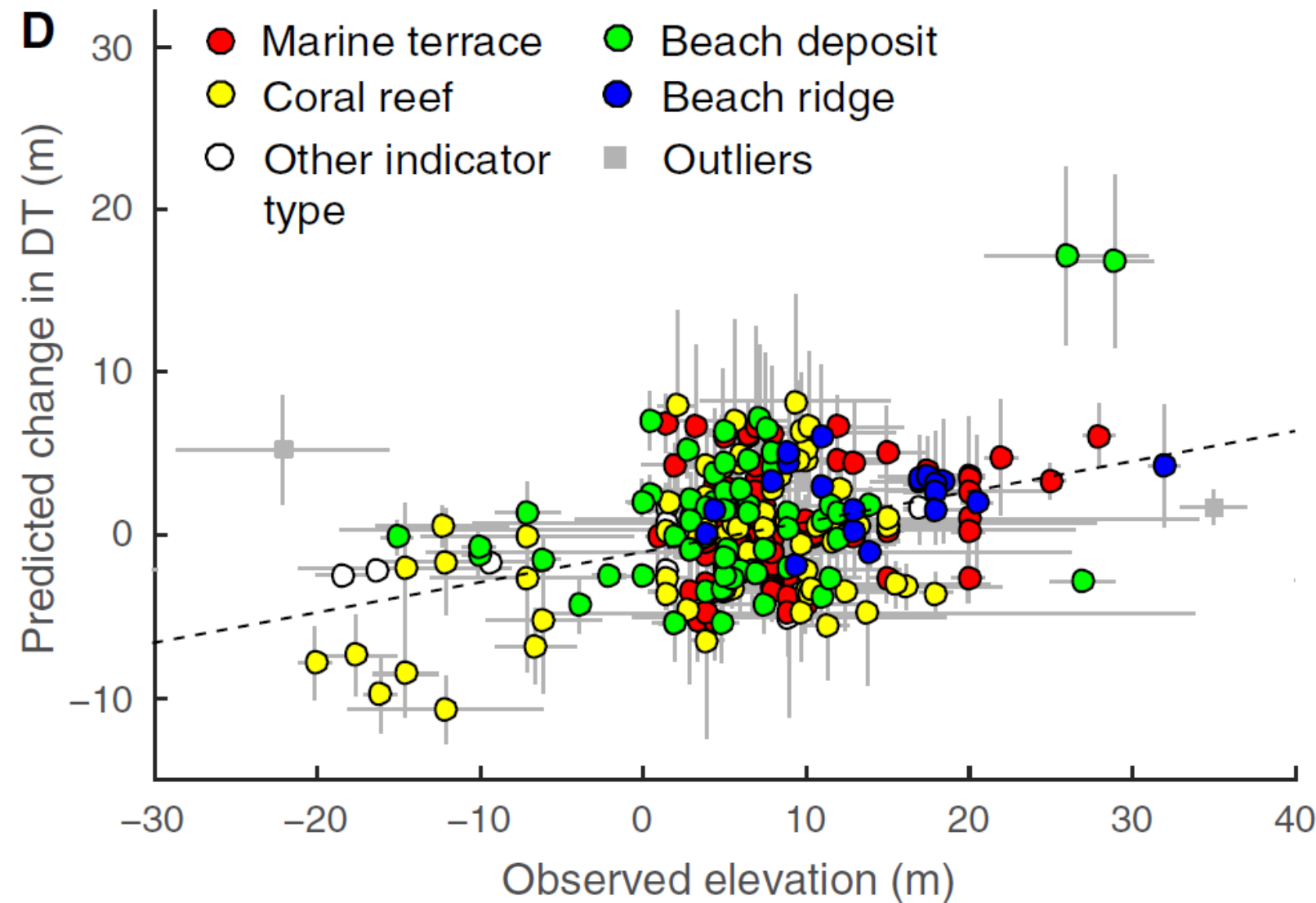


Modeling change in dynamic topography

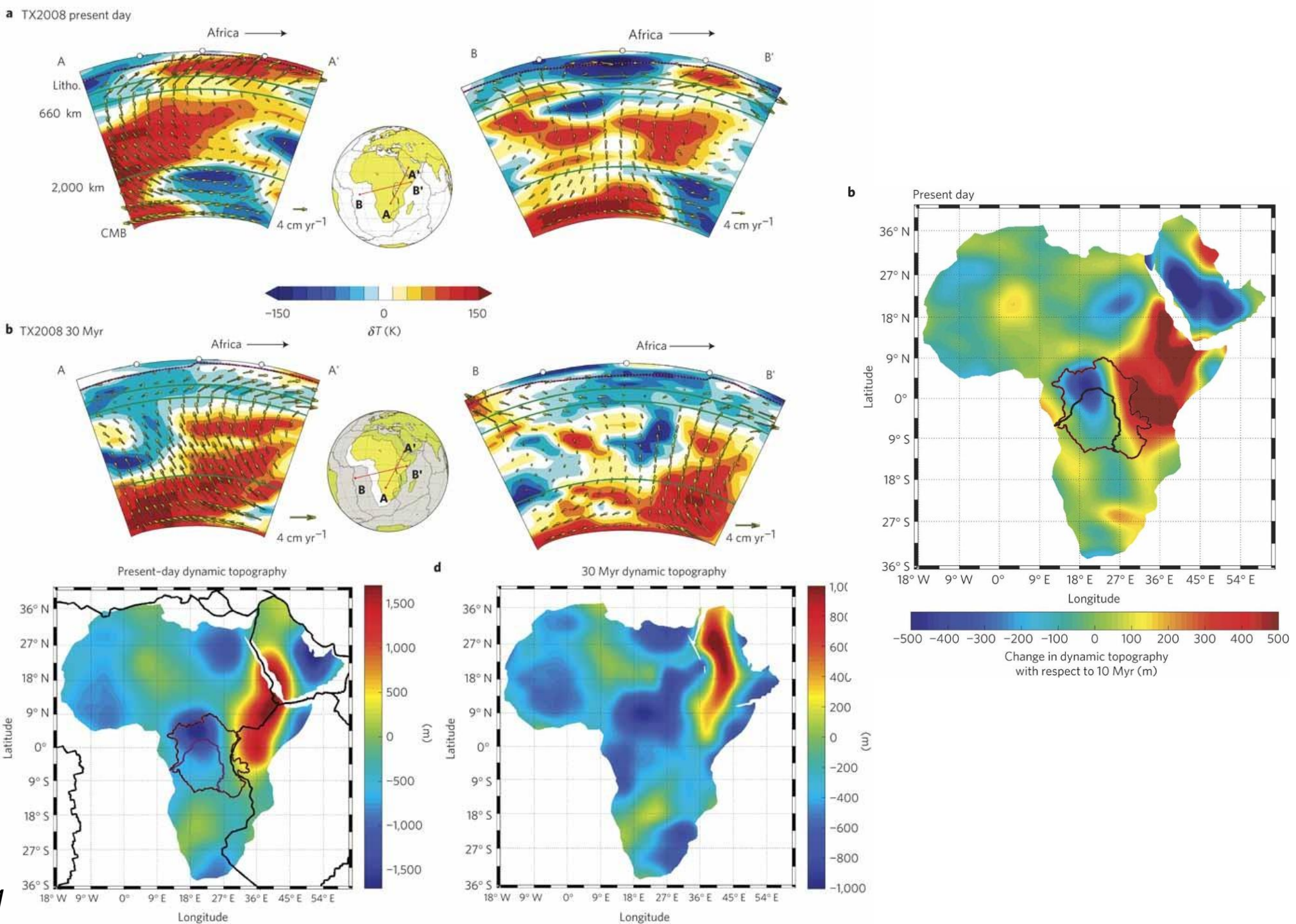
- (Quasi-)Instantaneous rate of change
- Time-dependent



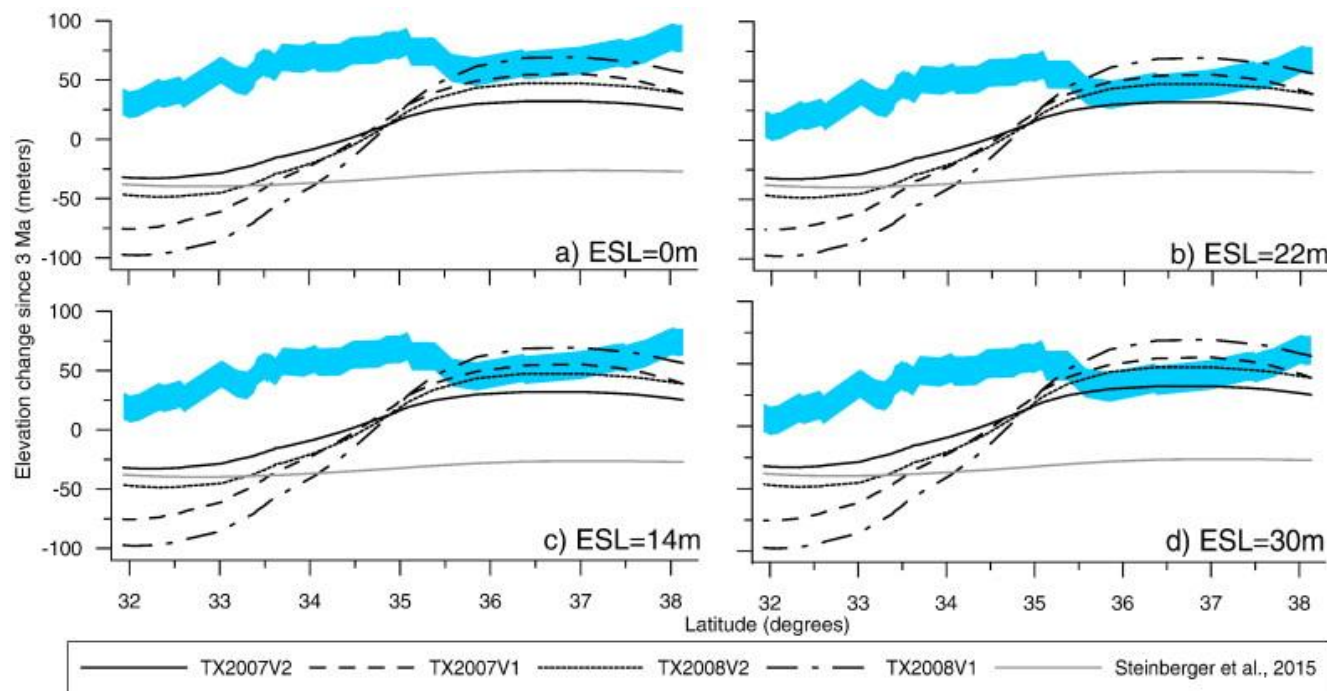
Average of 12 simulations



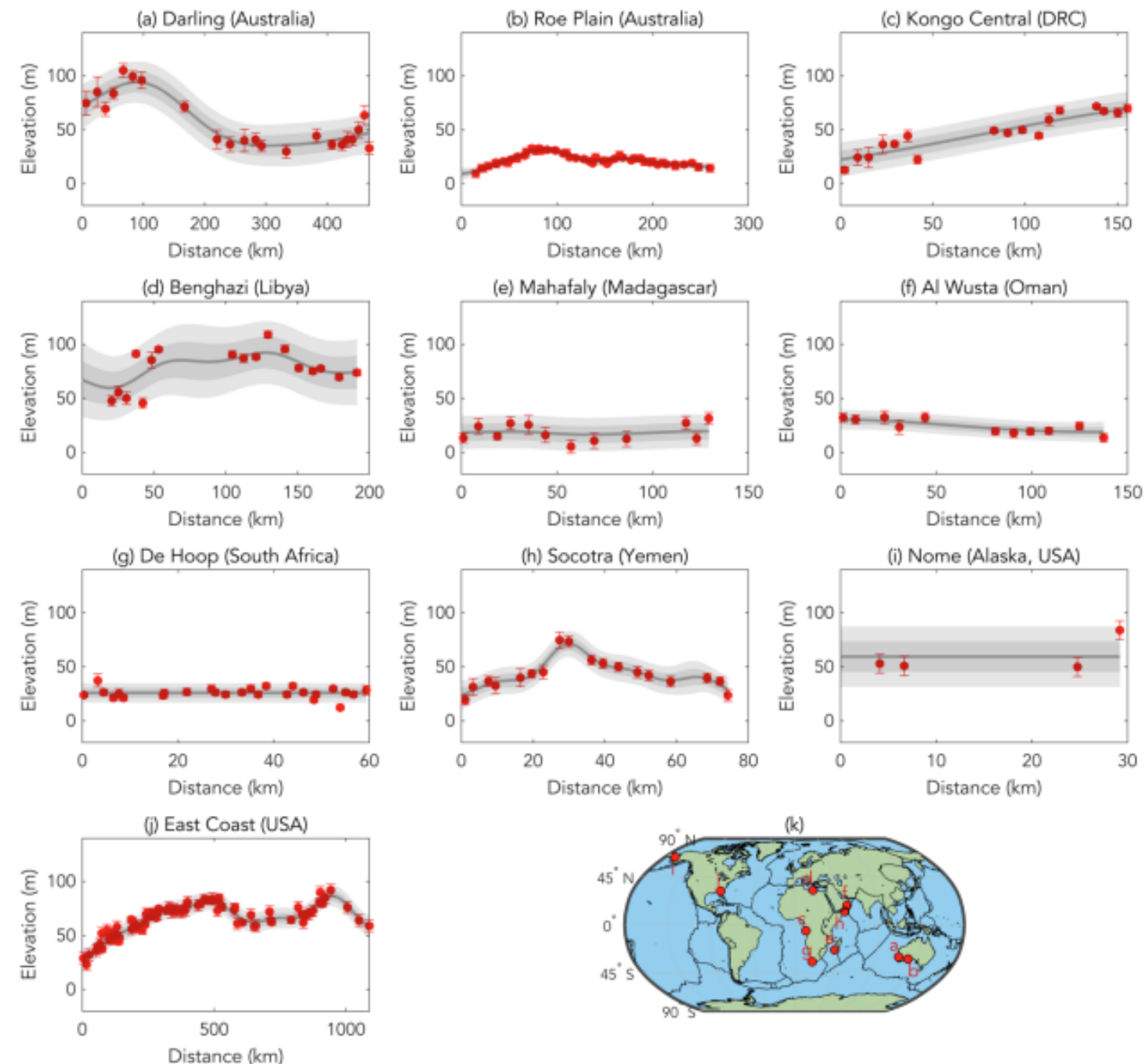
Ignoring thermal diffusion (assume high Rayleigh number), backwards advection



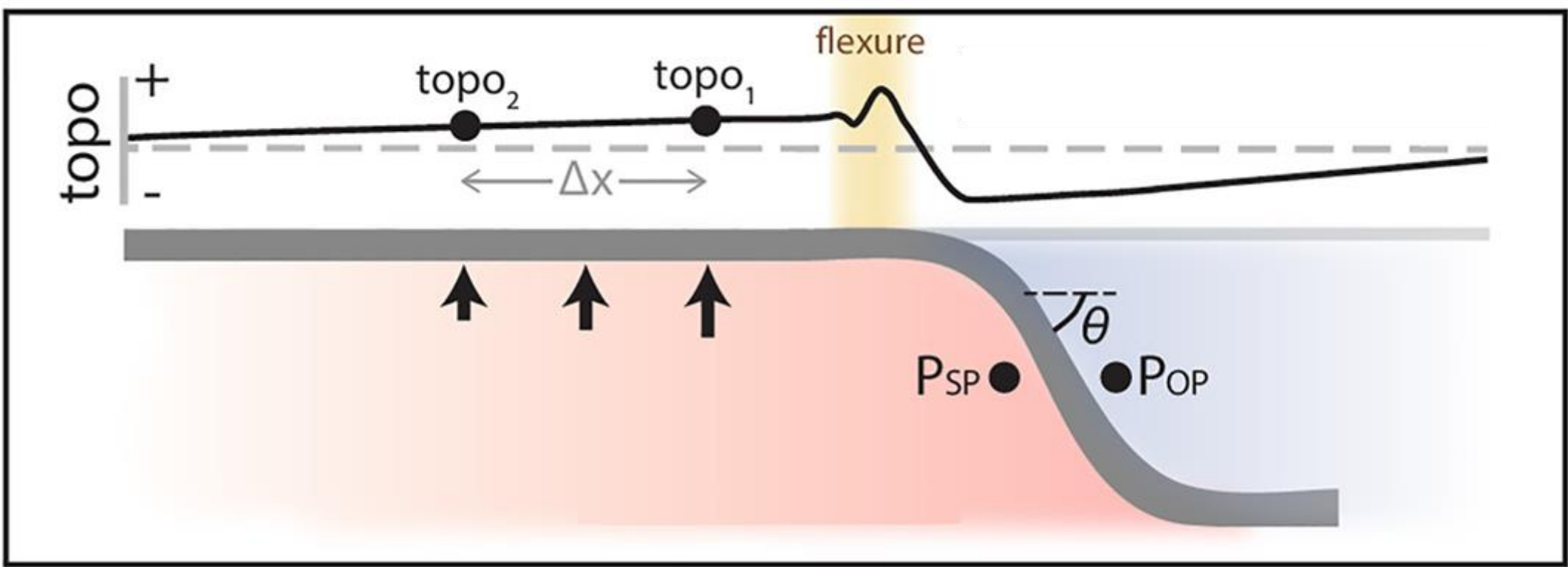
Orangeburg Scarp (3 Ma)

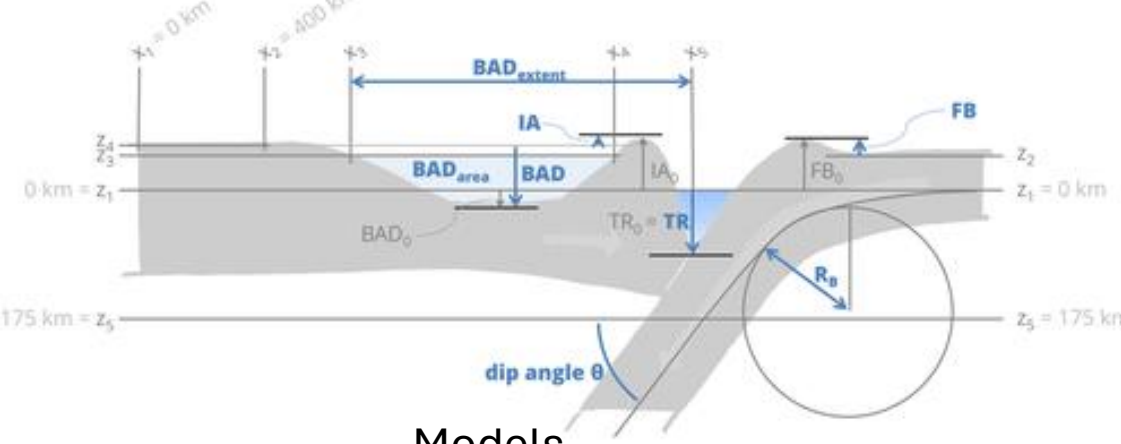


Ignoring thermal diffusion (assume high Rayleigh number), backwards advection

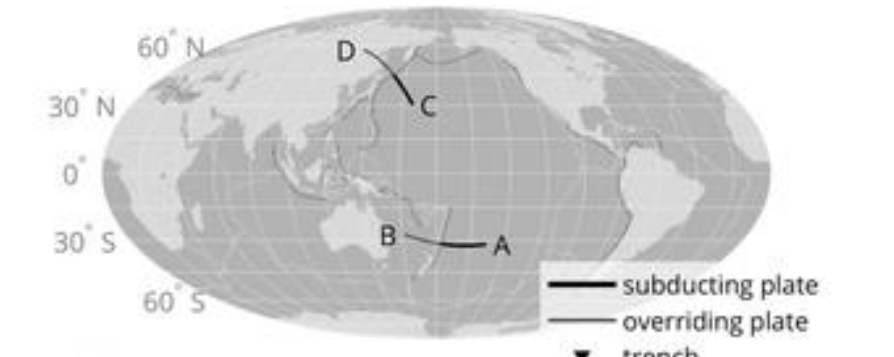
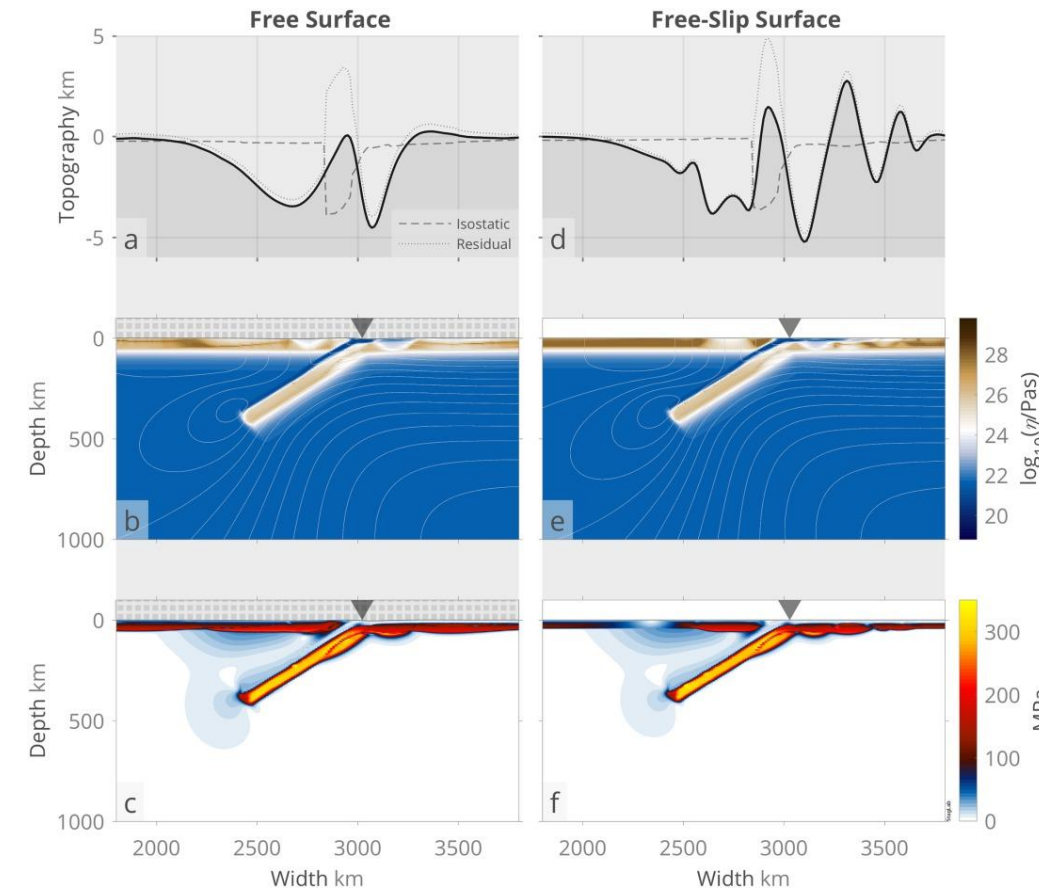


Subduction zone dynamic topography

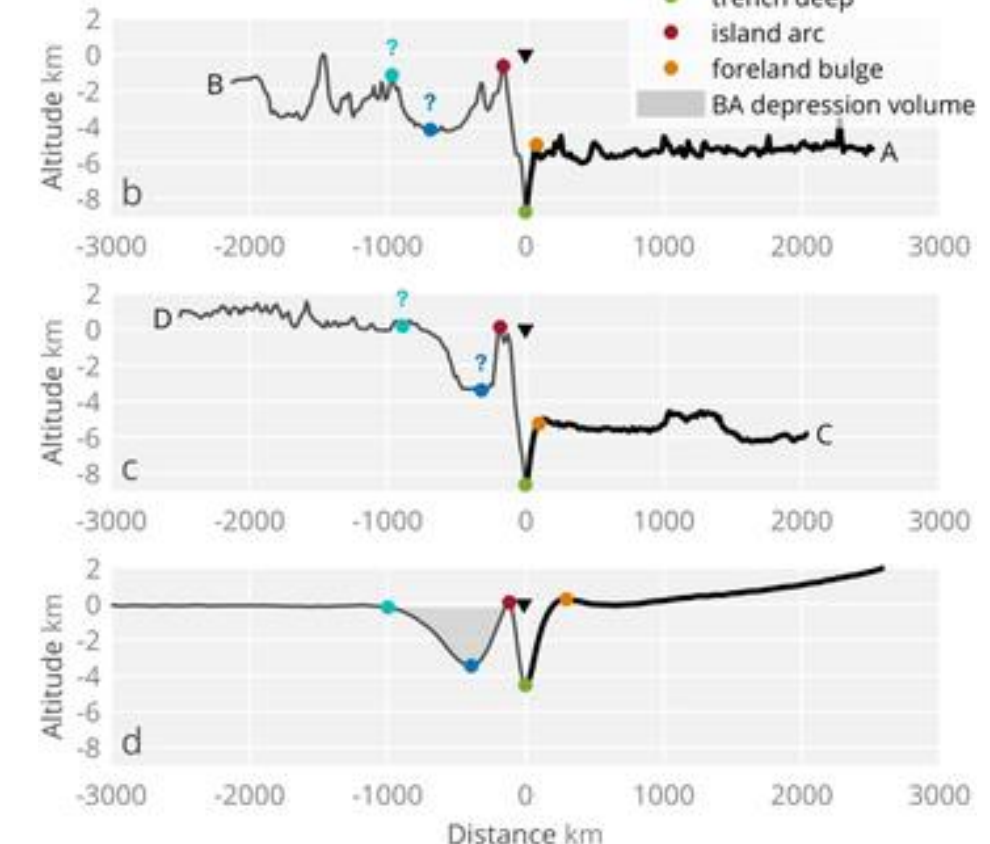


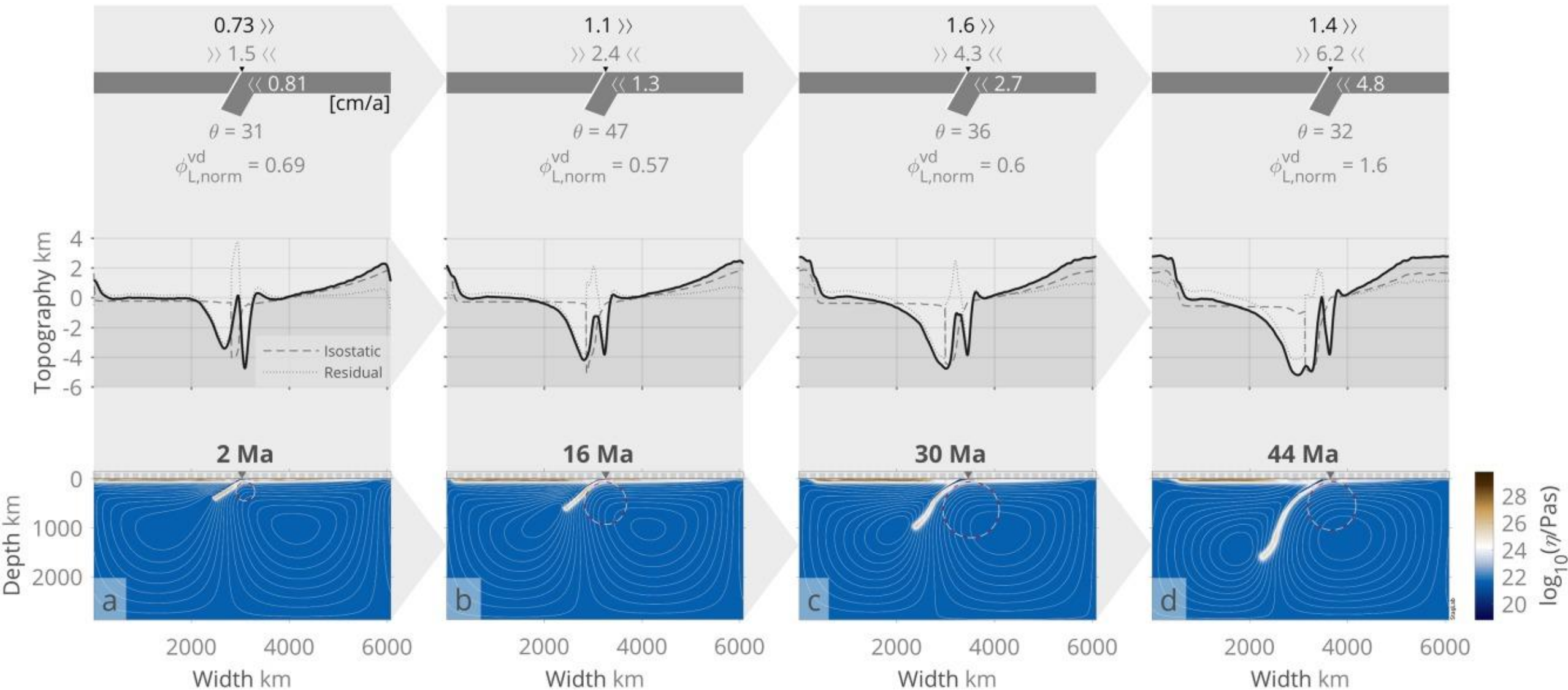


Models

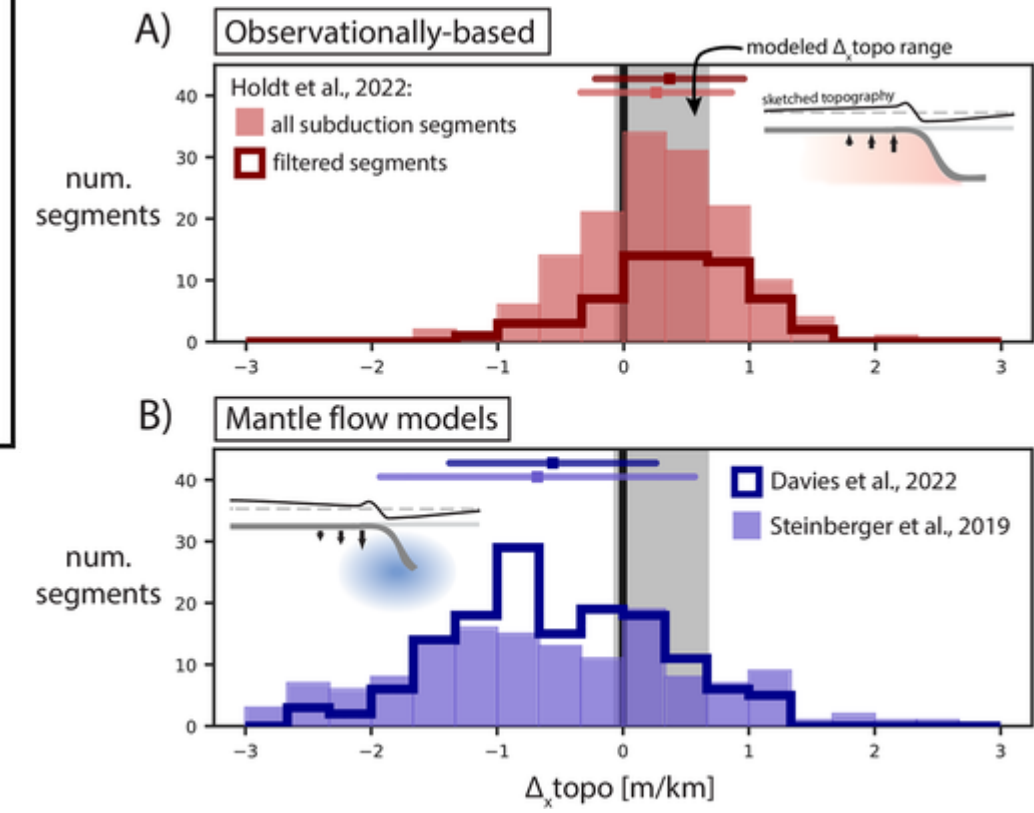
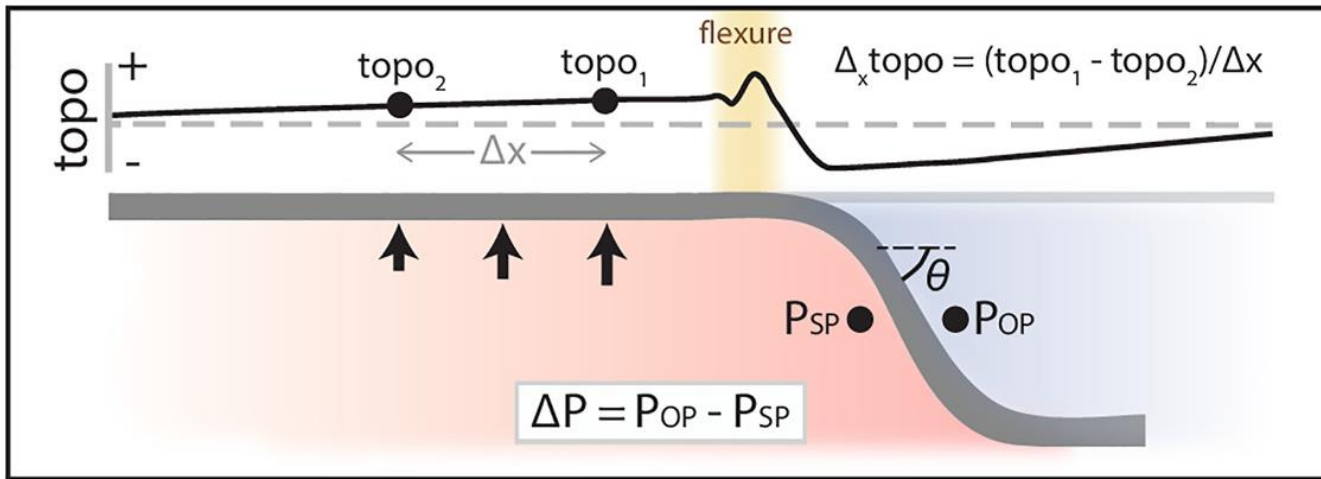


Observations





Subduction zone dynamic topography



Western Interior Seaway

130 Ma
(Early Cretaceous)



85 Ma
(Late Cretaceous)



60 Ma
(Paleogene)



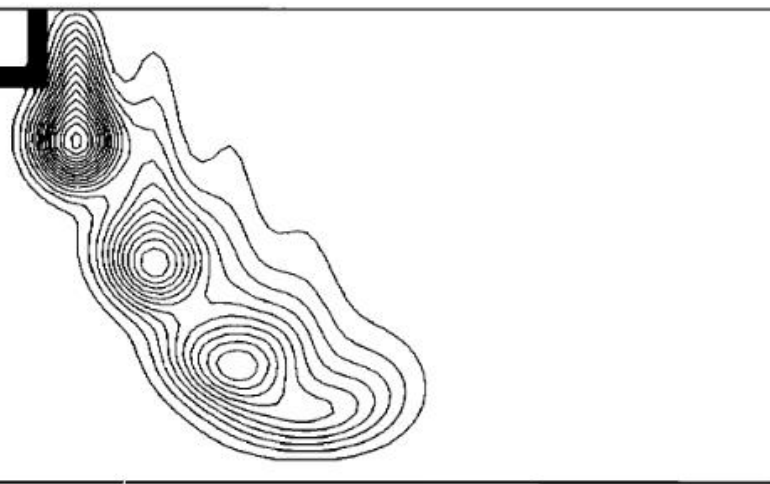


Fig. 10. The thermal field produced by superimposing the $t = 0.0, 0.25, 0.50, 0.75$, and 1.0 fields of the model of Figure 6 ($\Delta t = 0.25$, see text). Each field is horizontally shifted, with respect to the previous field, by an amount equal to the width of the initial block (116 km); only a portion of the cell is shown. The near-surface dip of the resulting subduction is approximately 45° .

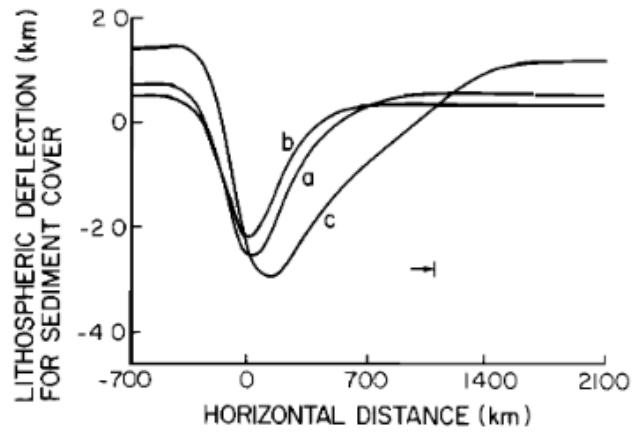


Fig. 11. The topographic profile corresponding to the field of Figure 10 (labeled a). Also shown are the deflections for the cases of near surface dips of 60° ($\Delta t = 0.33$, labeled b) and 30° ($\Delta t = 0.12$, labelled c). In all cases, $D = 5 \times 10^{23}$ Nm. The arrow gives the position of the right boundary of Figure 10.

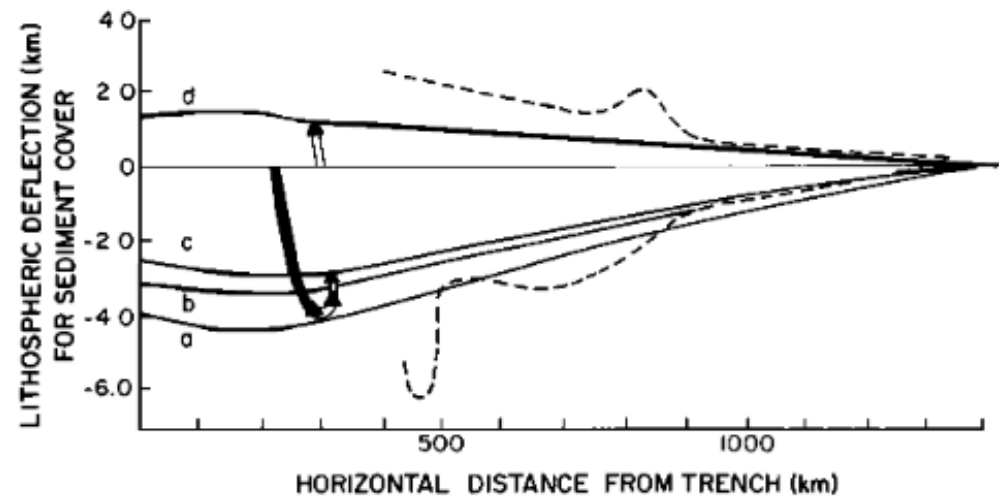
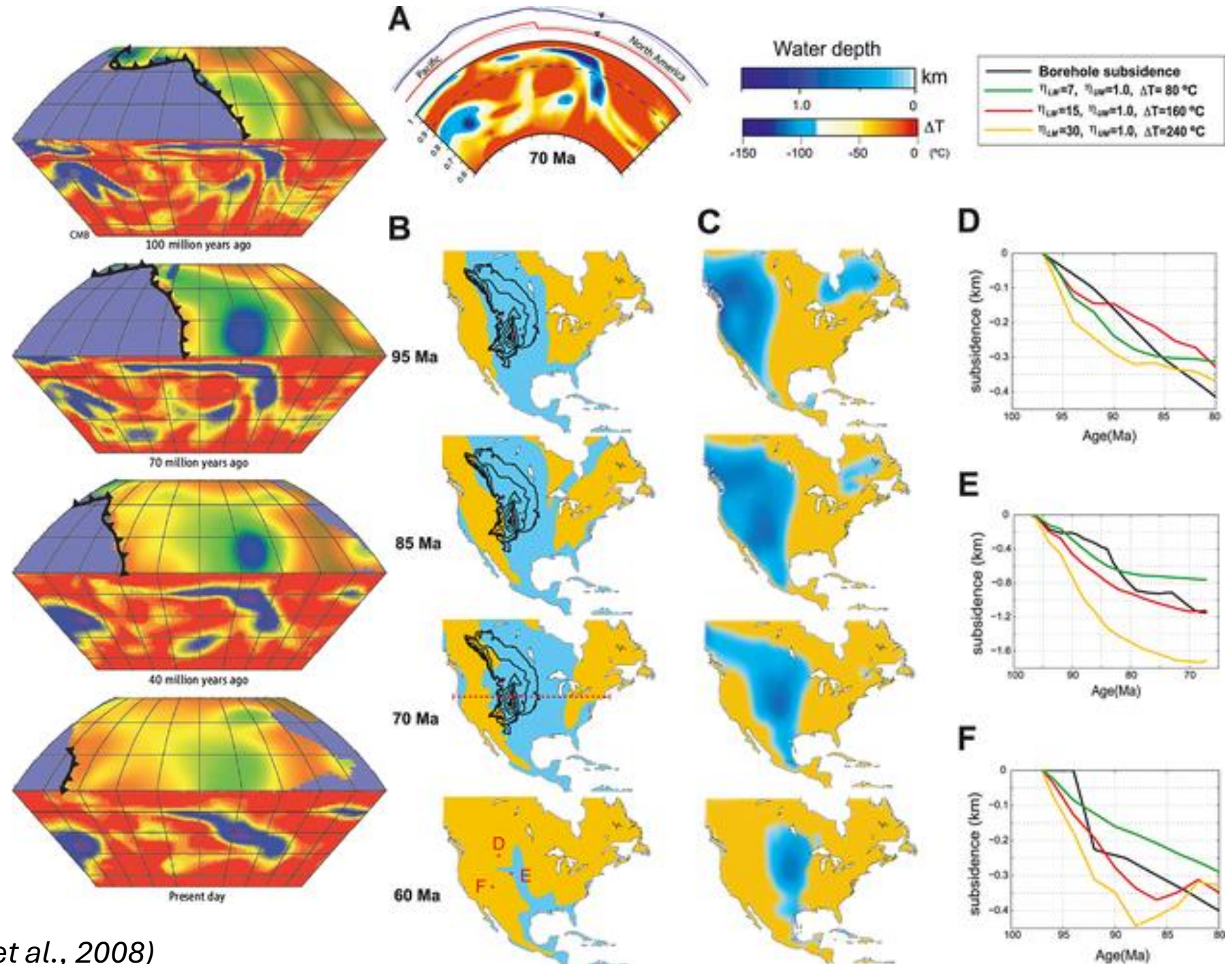
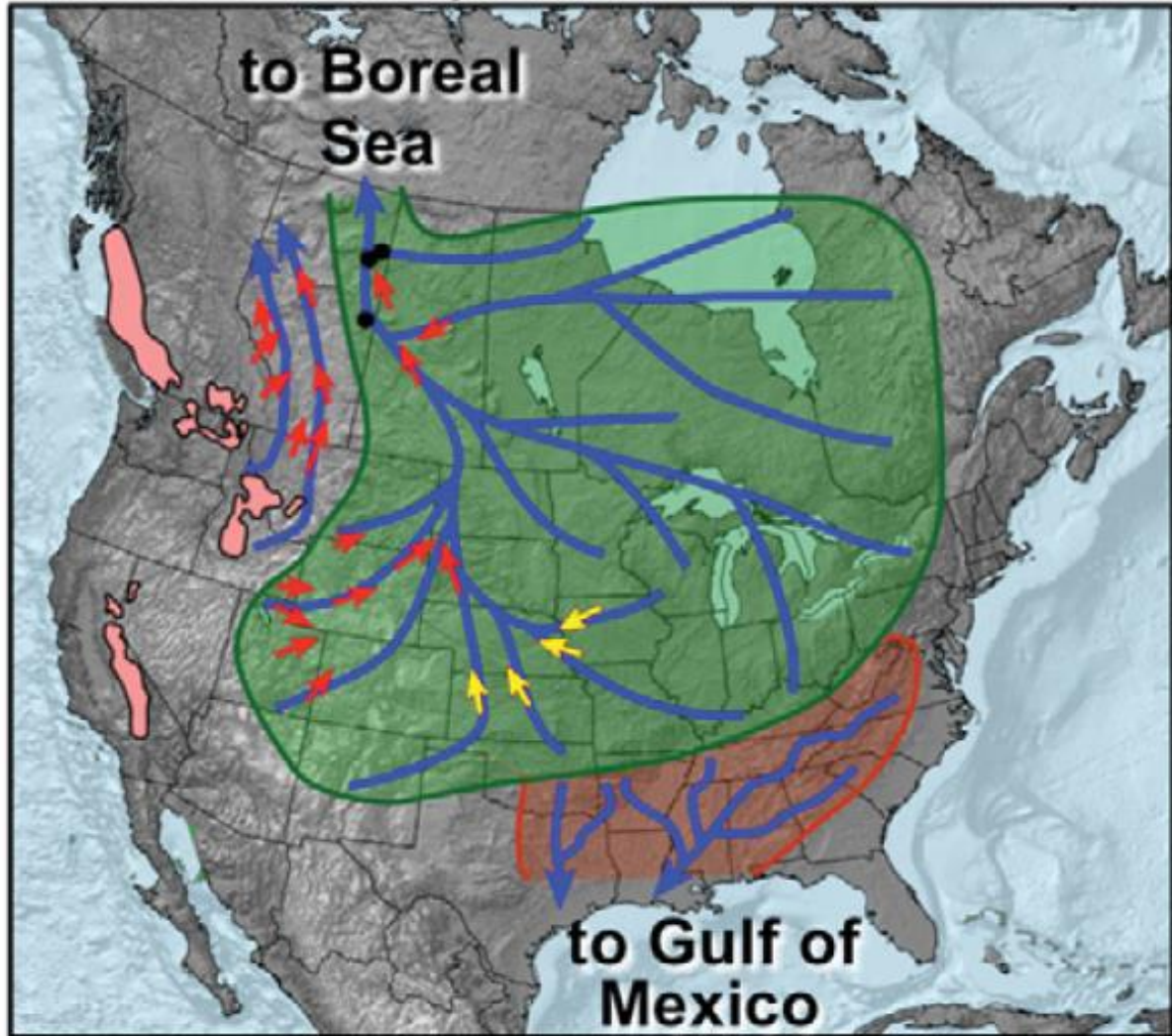


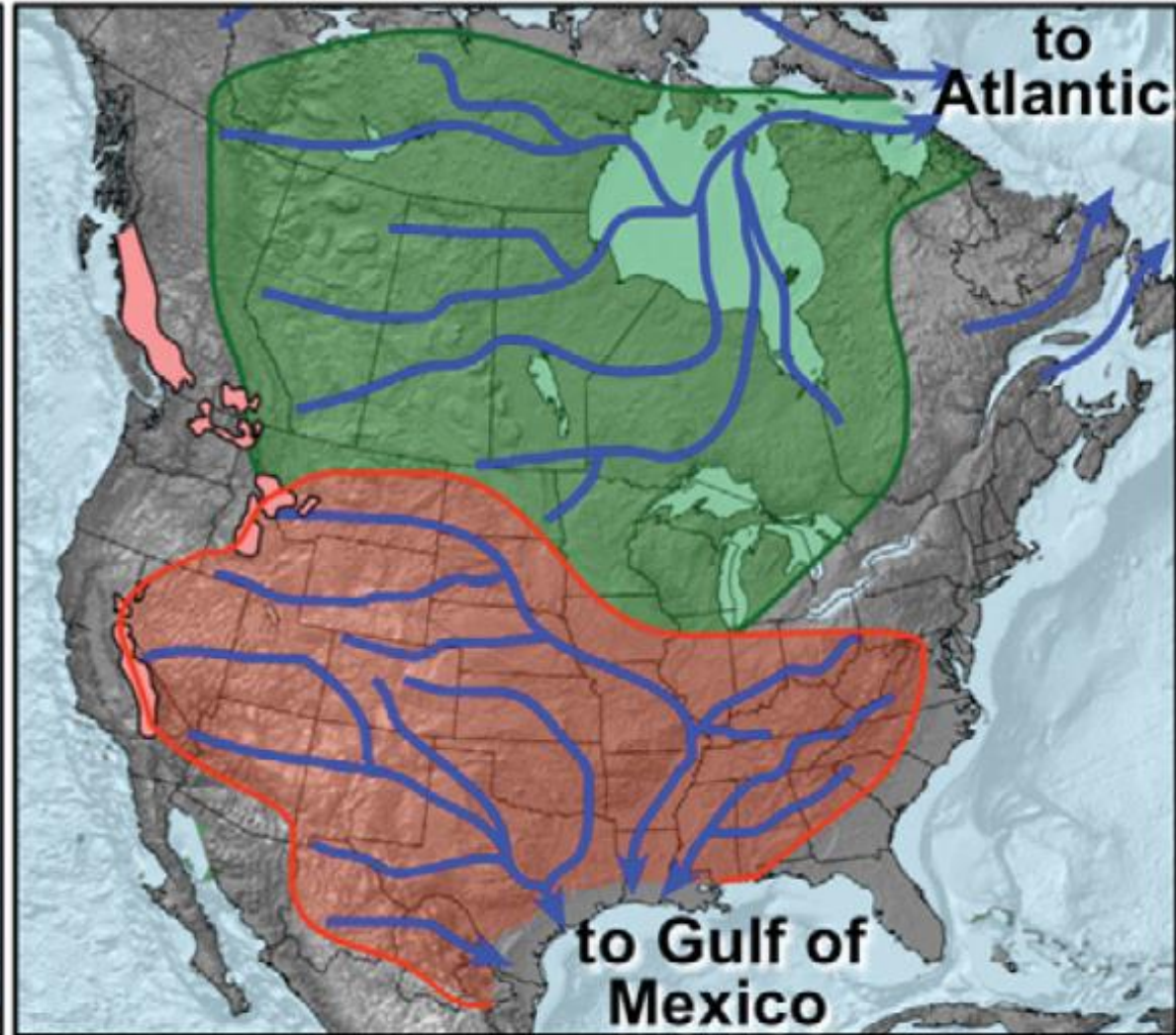
Fig. 15. Profile a, the lithospheric deflection profile corresponding to a model with block subduction, a dip of 25° , a near-surface temperature contrast of -700° K, and $D = 10^{24}$ Nm. a shows the maximum subsidence of the base of the sediment sequence. Profiles b and c are the corresponding results for the deflection 10 m.y. and 25 m.y., respectively, after subduction ceases at the surface. While the basement rebounds from a to c, the surface uplifts to d. Model predictions a and d should be compared with the corresponding observations (dashed lines) of Figure 5. Part of the observed subsidence and uplift between 400 and 900 km is probably caused by flexure under supracrustal overthrust loads. The baseline in this diagram is 250 m higher than the Late Cretaceous sea level. The topographic profiles are computed under the assumption that the sediment cover (of density 2.30×10^3 kg/m 3) remains intact subsequent to the onset of uplift.

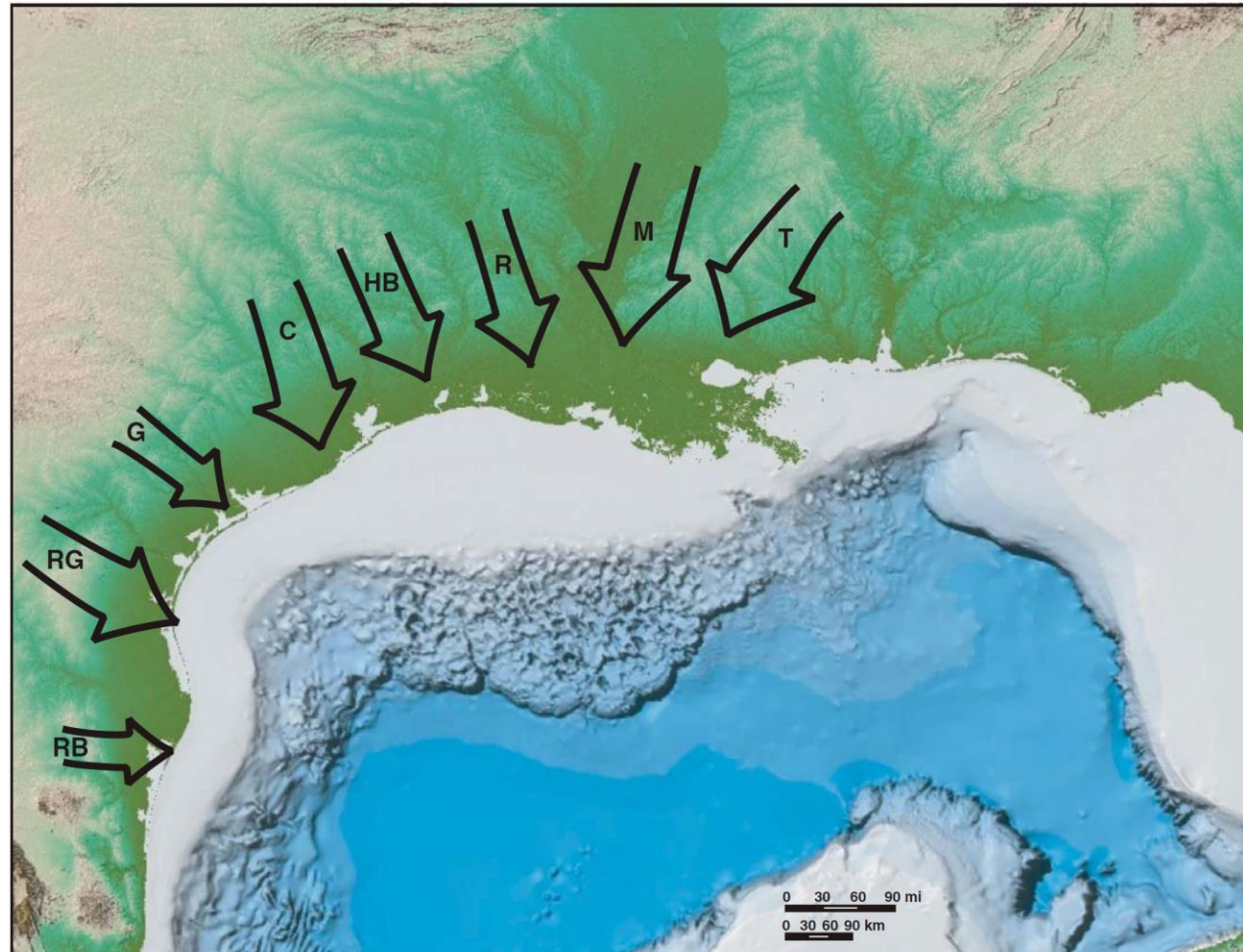
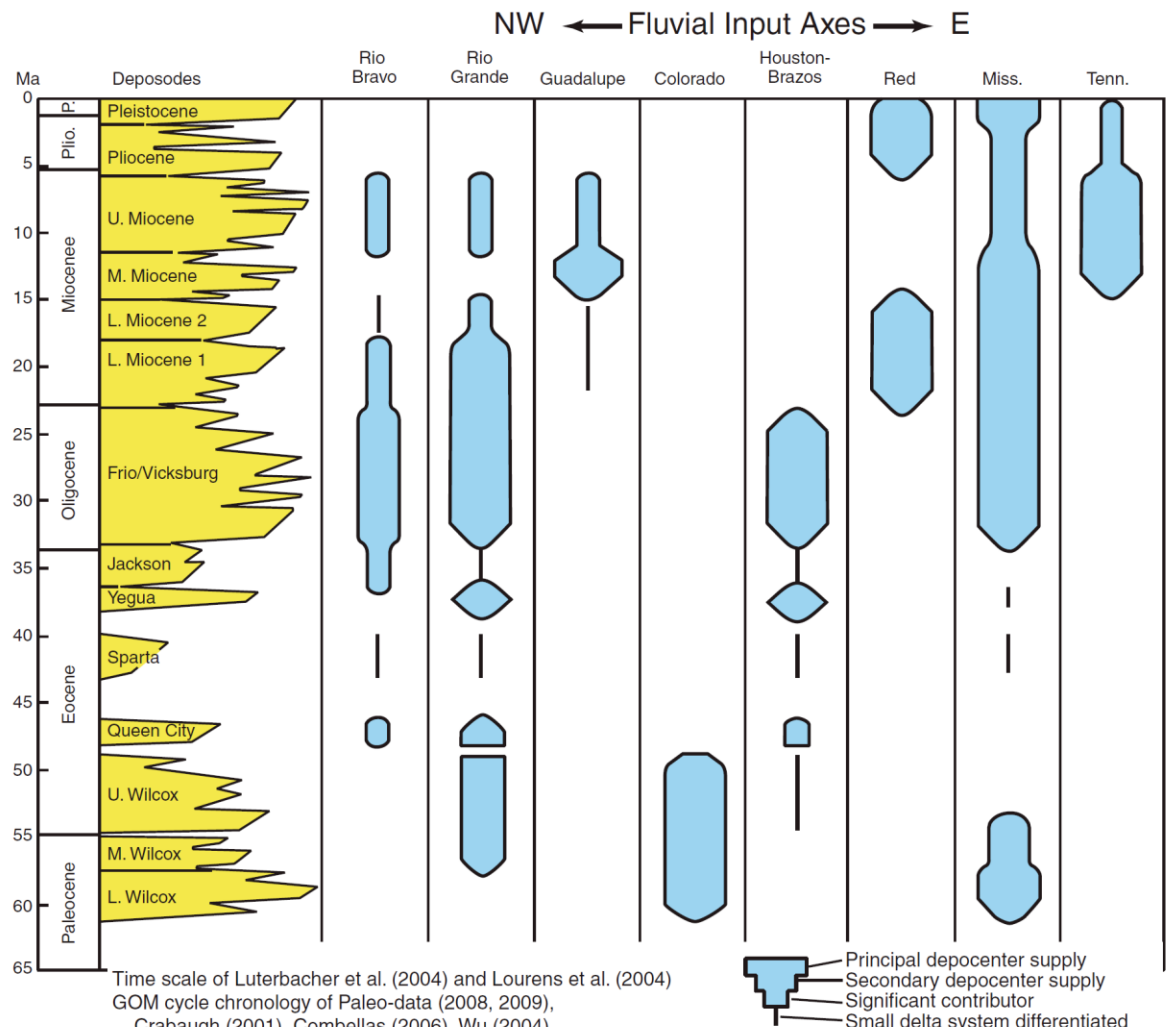


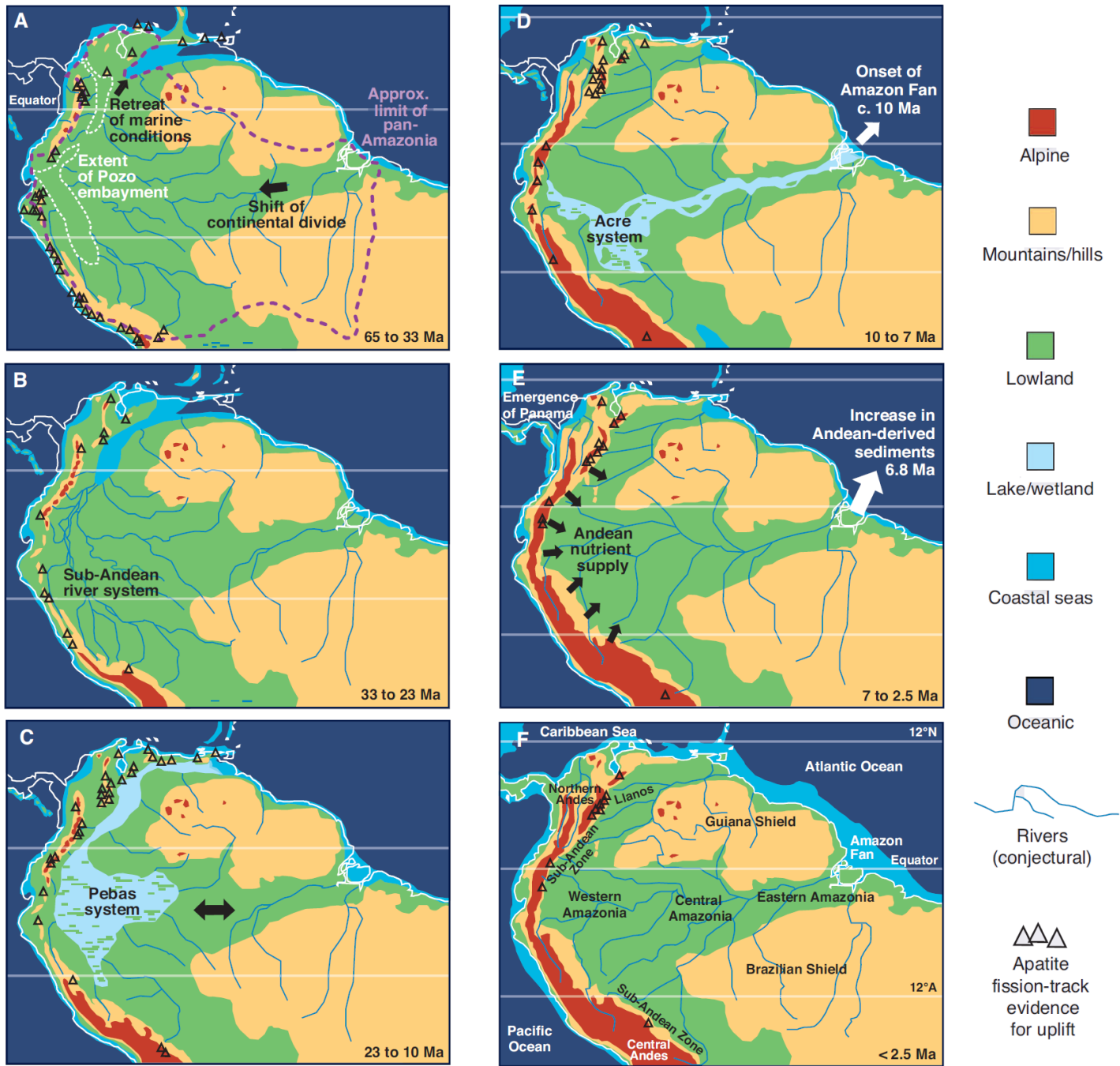
Early Cretaceous



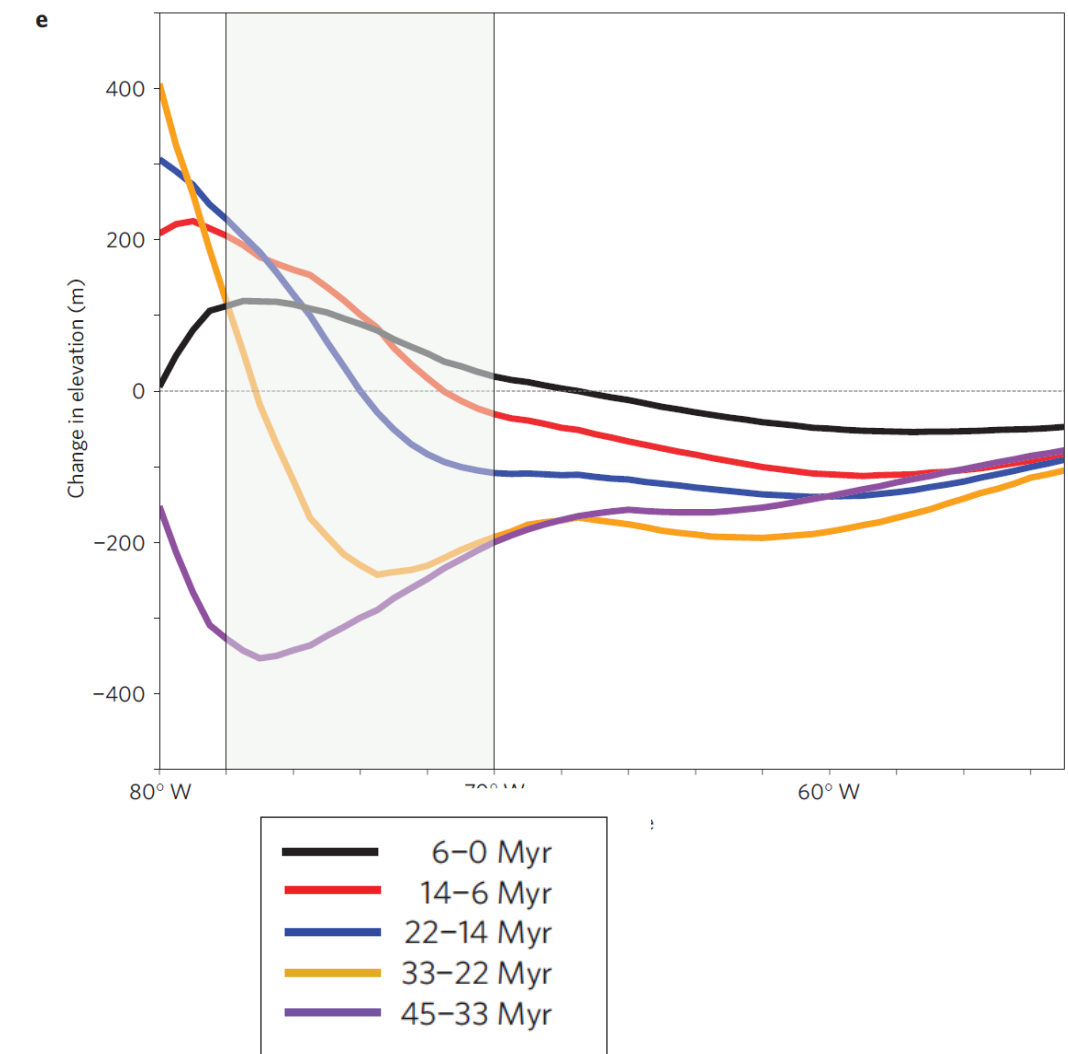
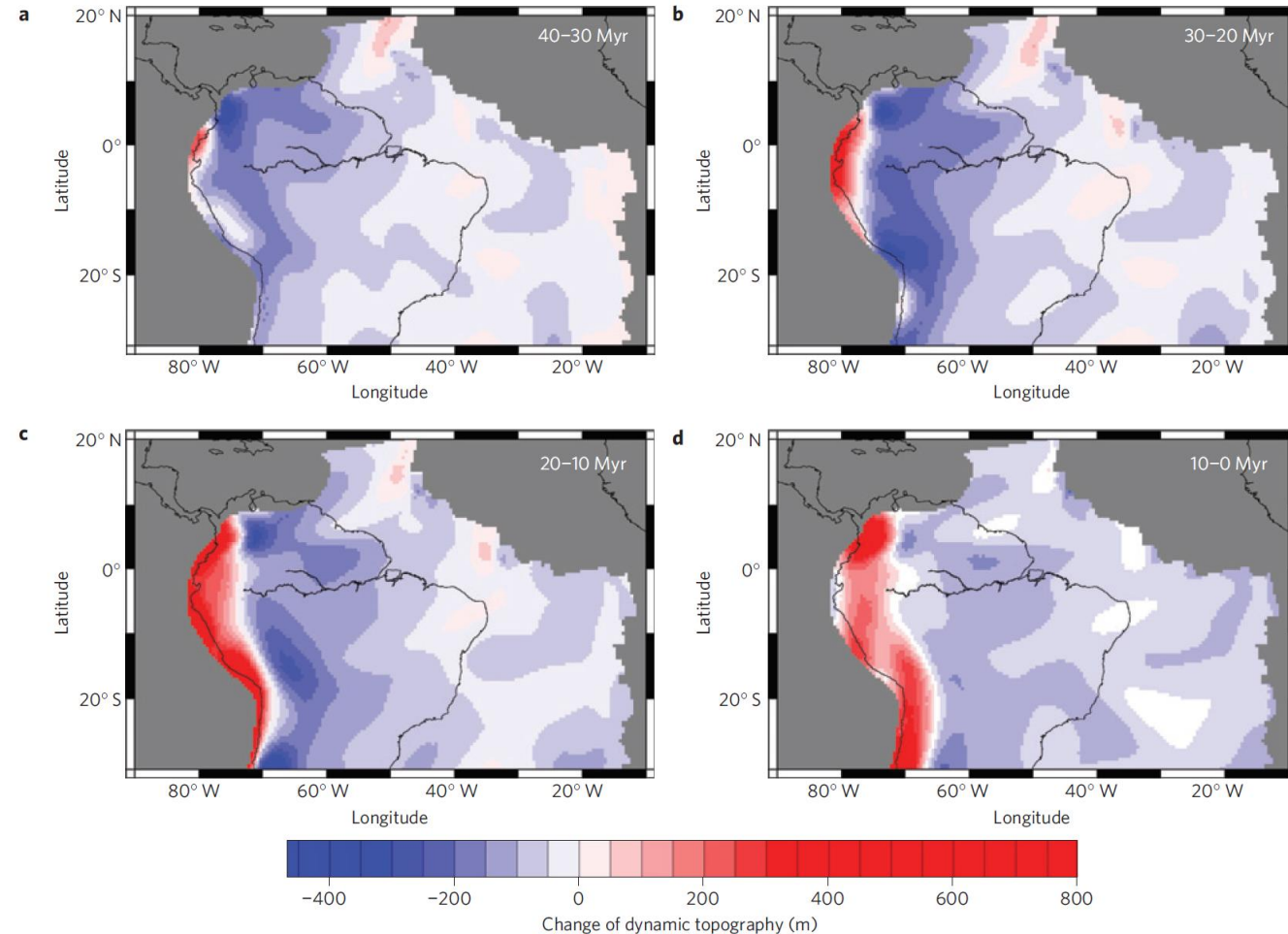
Paleocene



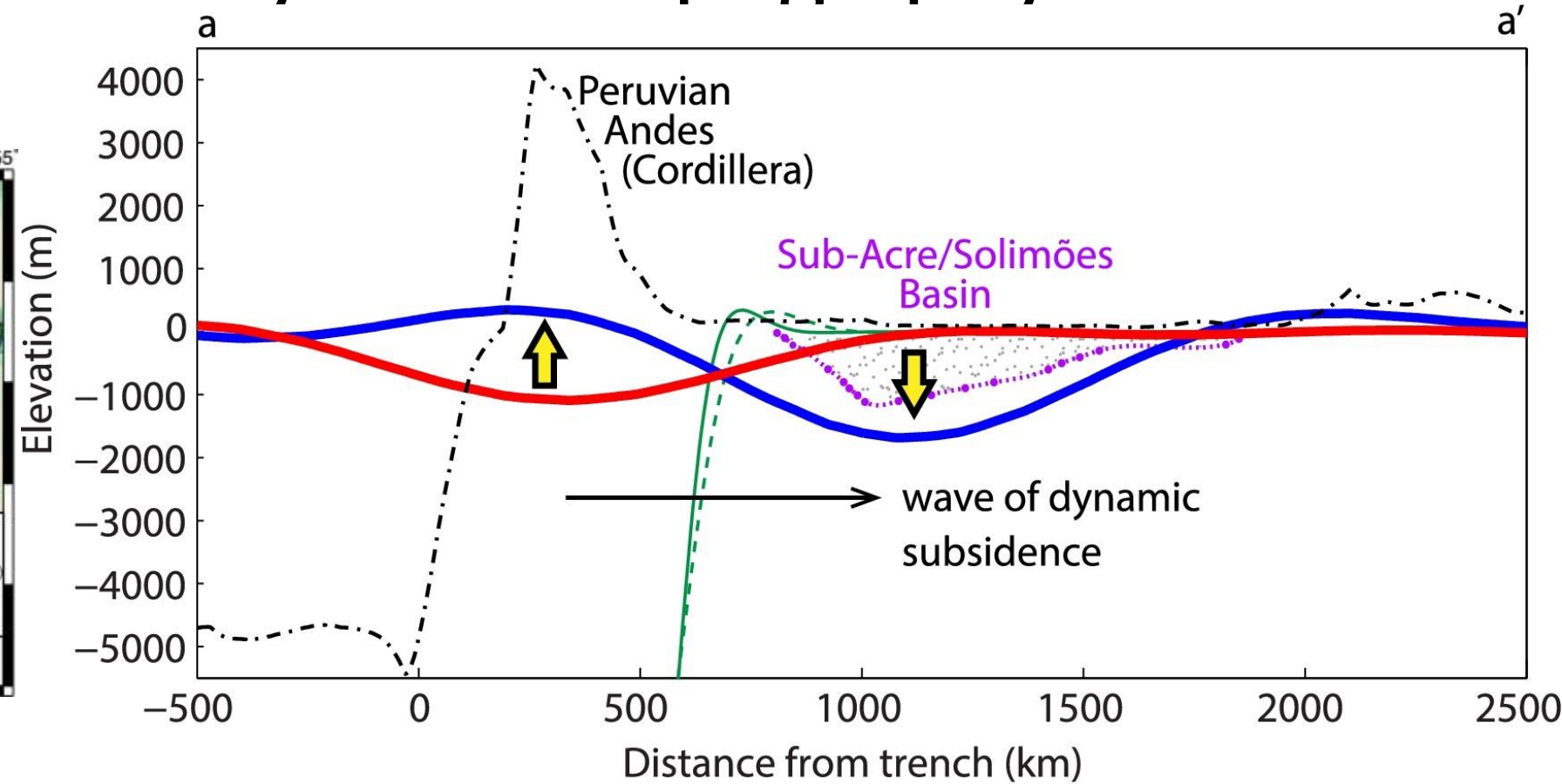
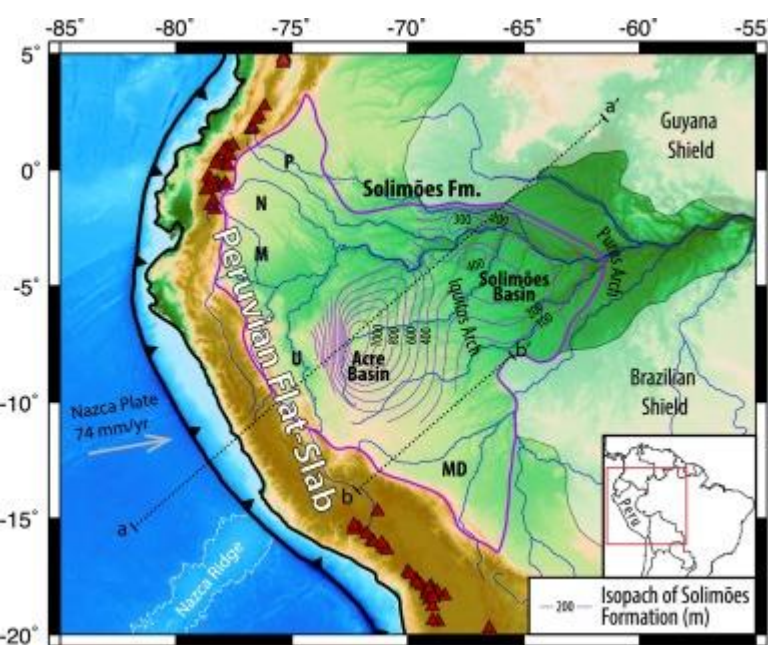




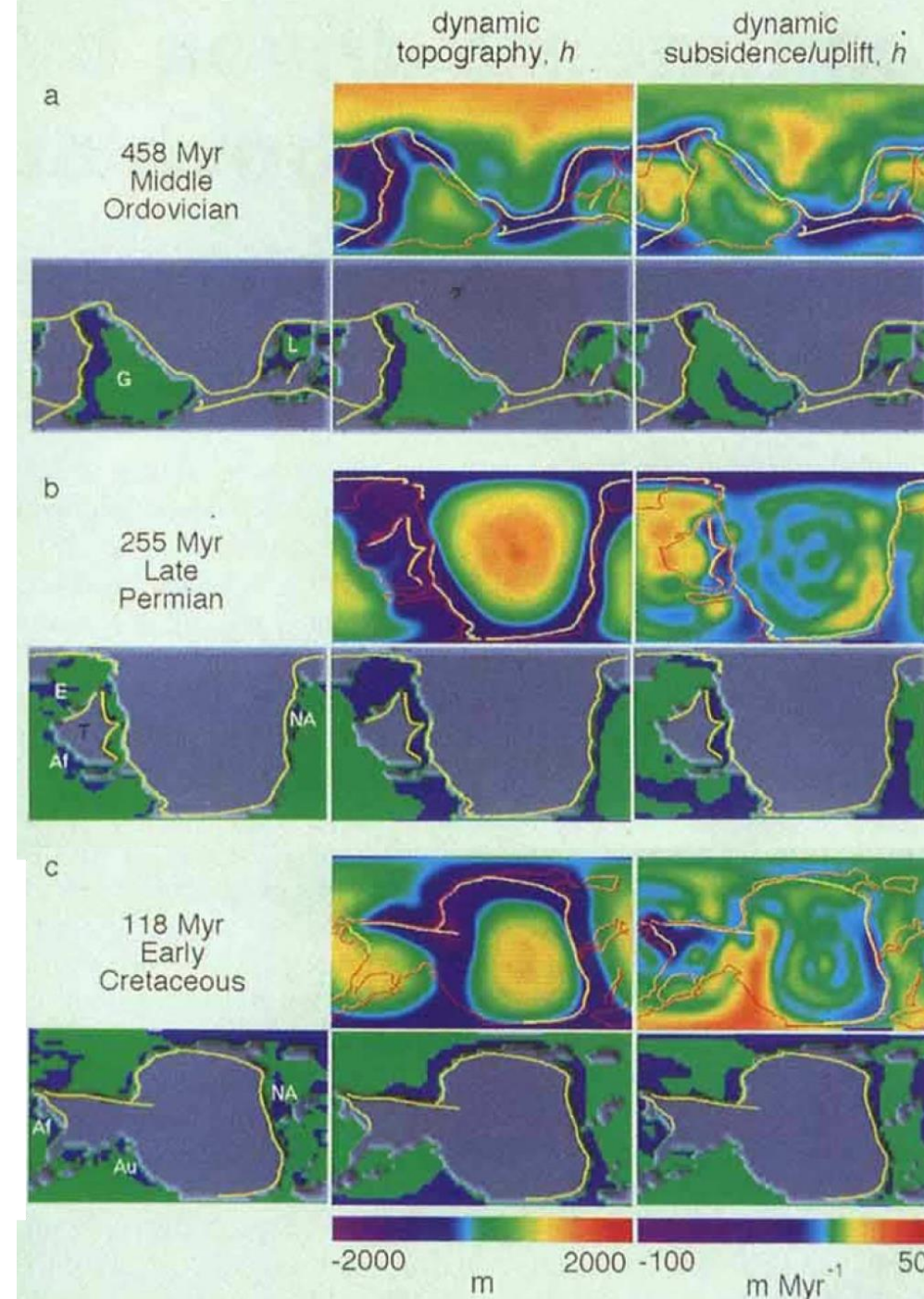
South American Dynamic Topography



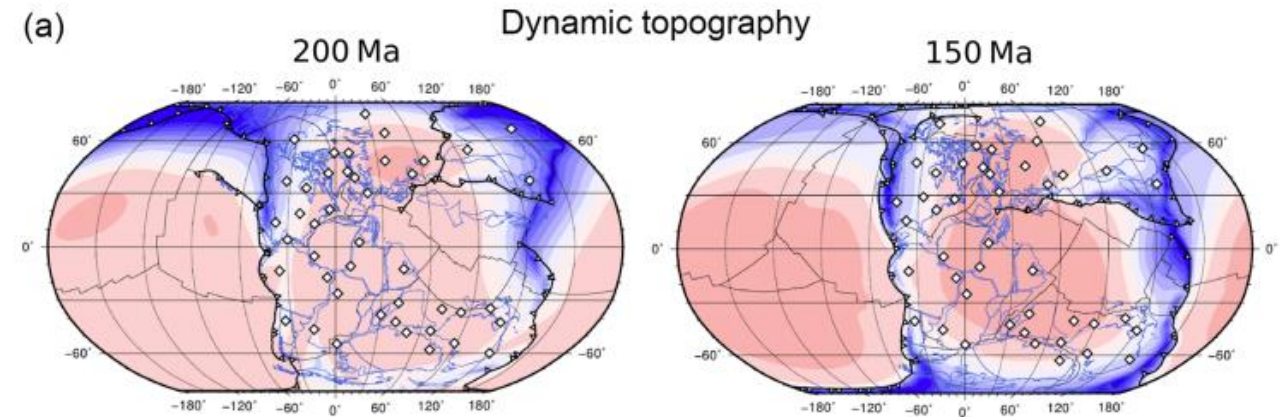
South American Dynamic Topography



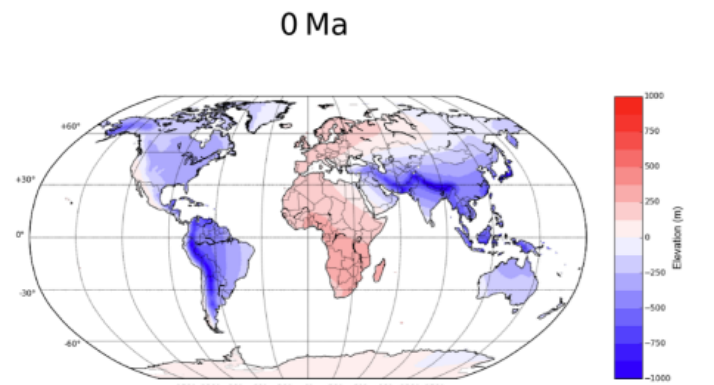
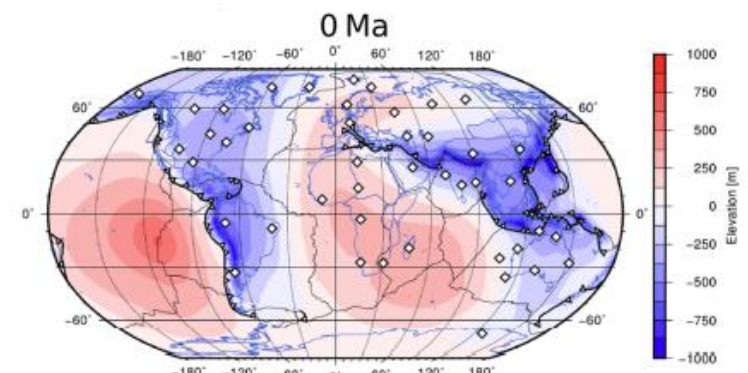
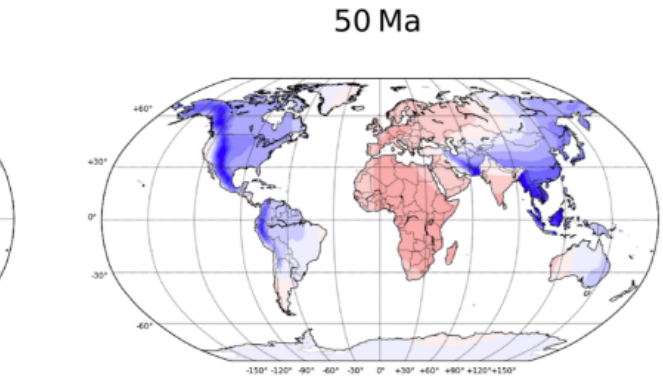
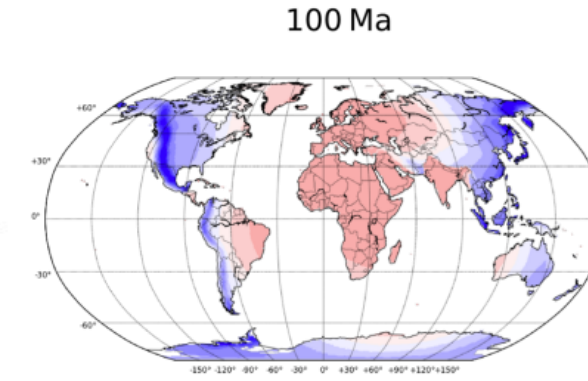
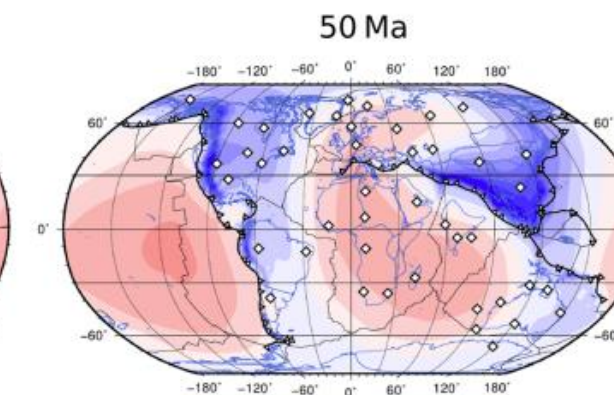
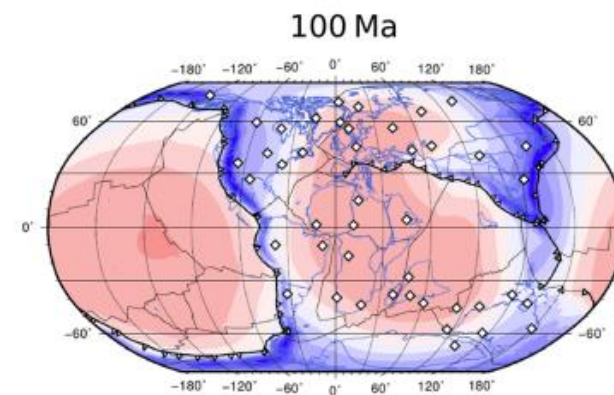
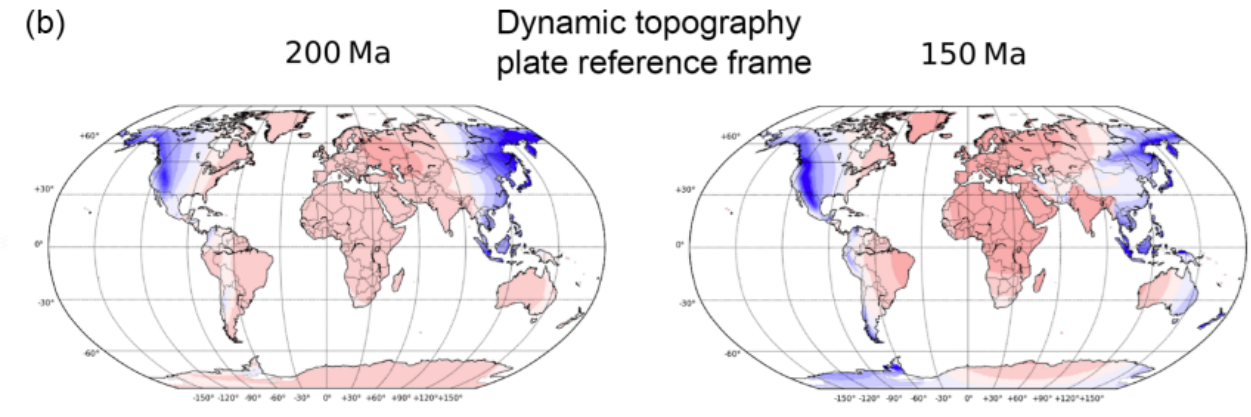
--- topography — flexure 25km Te - - - flexure 40km Te basin depth
— flat-slab dynamic topography — normal-slab dynamic topography
↓ relative dynamic topography due to flat-slab arrival



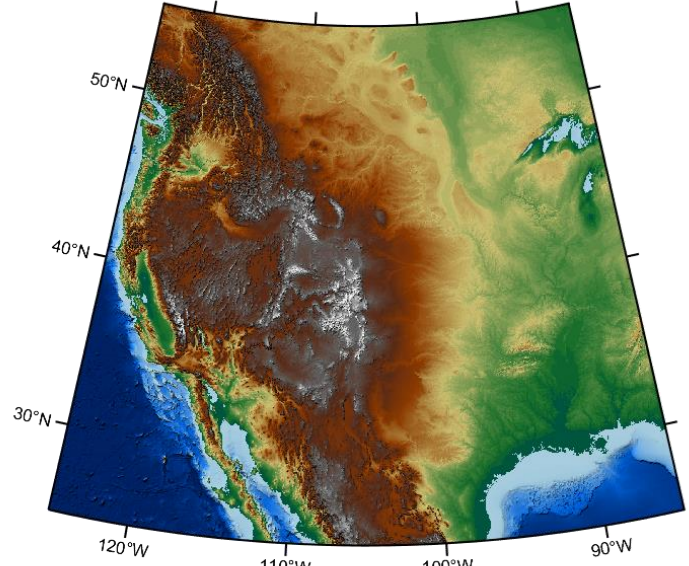
(a)



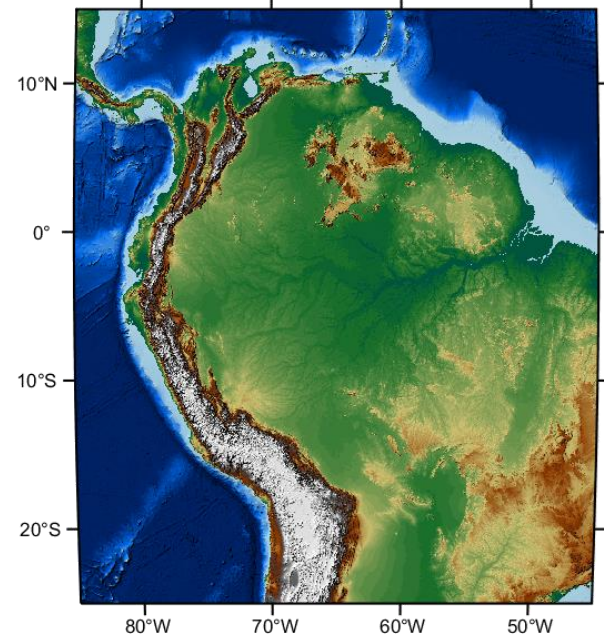
(b)



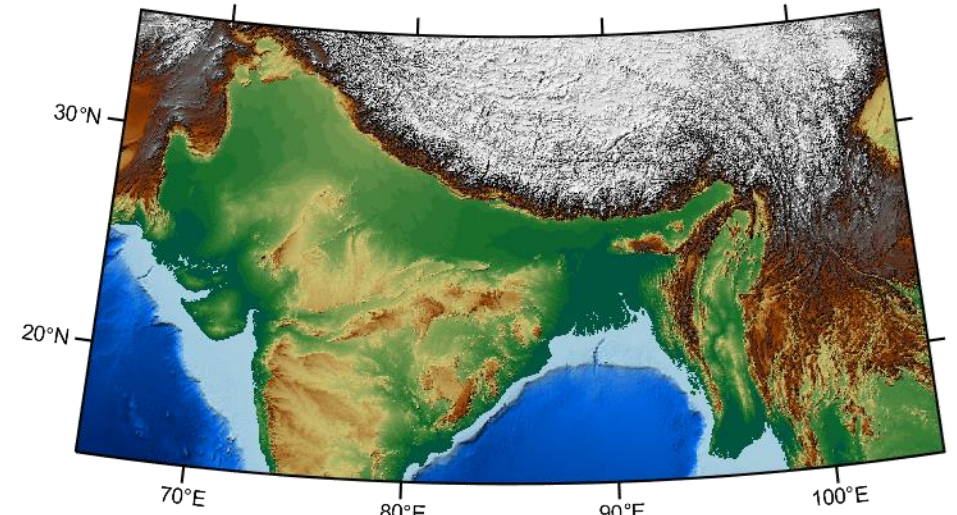
Overfilled



Orogen-transverse drainage



Underfilled



Orogen-parallel drainage

